PHYSICAL REVIEW FLUIDS **8**, 044601 (2023)

Shock impingement on a transitional hypersonic high-enthalpy boundary layer

D. Passiatore,[1,*] L. Sciacovelli,[2] P. Cinnella,[3] and G. Pascazio[4]
[1]*DMMM, Politecnico di Bari, via Re David 200, 70125 Bari, Italy*
[2]*Laboratoire DynFluid, Arts et Métiers ParisTech, 151 Bd. de l'Hôpital, 75013 Paris, France*
[3]*Sorbonne Université, Institut Jean Le Rond d'Alembert, 4 Place Jussieu, 75005 Paris, France*
[4]*DMMM, Politecnico di Bari, via Re David 200, 70125 Bari, Italy*

(Received 13 December 2022; accepted 30 March 2023; published 17 April 2023)

The dynamics of a shock wave impinging on a transitional high-enthalpy boundary layer out of thermochemical equilibrium is investigated by means of a direct numerical simulation. The freestream Mach number is equal to 9, and the oblique shock impinges with a cooled flat-plate boundary layer with an angle of 10°, generating a reversal flow region. In conjunction with freestream disturbances, the shock impingement triggers a transition to a fully turbulent regime shortly downstream of the interaction region. Accordingly, wall properties emphasize the presence of a laminar region, a recirculation bubble, a transitional zone, and a fully turbulent region. In the entire transitional process, the recognized mechanisms are representative of the second mode instability combined with stationary streaky structures, their destabilization being eventually promoted by shock impinging. The breakdown to turbulence is characterized by large increases of skin friction and wall heat flux, due to the particular shock pattern. At the considered thermodynamic conditions the flow is found to be in a state of thermal nonequilibrium throughout the computational domain. Overall, the dynamics of the interaction is little affected by thermal nonequilibrium effects; on the contrary, the latter are enhanced and sustained by the shock-induced laminar/turbulent transition, while chemical activity is almost negligible due to wall cooling. In the interaction region, relaxation towards thermal equilibrium is delayed, and the fluctuating values of the rotranslational and the vibrational temperatures strongly differ, despite the wall cooling. The fully turbulent portion exhibits evolutions of streamwise velocity, Reynolds stresses, and turbulent Mach number in good accordance with previous results for highly compressible cooled-wall boundary layers in thermal nonequilibrium, with turbulent motions sustaining thermal nonequilibrium. Nevertheless, the vibrational energy is found to contribute minimally to the total wall heat flux.

DOI: 10.1103/PhysRevFluids.8.044601

I. INTRODUCTION

Shock-wave boundary layer interactions (SWBLIs) have been extensively investigated over the last few decades due to their importance for both aeronautical and aerospace applications. The impingement of a shock wave on a fully developed boundary layer may occur for several reasons and in both internal and external flow configurations. For instance, a shock wave interacting with a boundary layer can be driven by the complex geometry of the body itself (e.g., ramps, wedges), or it can impinge on the boundary layer after generating from an external body. The latter can be

---

[*] Present address: Center for Turbulence Research, Stanford University, Stanford, CA 94305, USA; Corresponding author: donatella.passiatore@poliba.it.

the case of supersonic intakes or multibody launch vehicles, and it is the focus of the present work. The physics underlying such configuration is complex and strongly multiscale. The dynamics of high-speed compressible turbulent boundary layers becomes tightly coupled with strong gradients of the thermodynamic properties, leading to an increase of thermomechanical loads (see, e.g., [1] for an overview of relevant physical processes). In hypersonic and high-enthalpy regimes, thermochemical nonequilibrium effects (i.e., chemical reactions and vibrational excitation) must be taken into account as well [2], further complicating the picture. Given the coexistence of several critical features, computational approaches based on averaged Navier-Stokes equations are unable to faithfully predict the flow field behavior, hence the necessity of performing high-fidelity spatial- and time-resolving simulations.

When an incident shock impinges on a fully developed boundary layer, the latter experiences a strong adverse pressure gradient. If the shock is strong enough, a recirculation bubble occurs and the flow separates. Several additional flow features are generated by this interaction, depending on the nature of the incoming boundary layer. Laminar boundary layers have the advantage of a lower drag but are more sensitive to separation in adverse pressure gradients, resulting in wider recirculation bubbles with respect to turbulent flows. In such configurations, investigations have been carried out concerning shock-induced instabilities [3,4] as well as shock-induced transition to turbulence [5], which can be obtained when the shock angle is sufficiently high.

The interaction between an oblique shock and a fully turbulent boundary layer has been the object of intensive research efforts [6–11]. One of the most remarkable results of the interaction is the amplification of turbulence downstream of the incident shock and the emergence of oscillatory motions. For strong interactions, the ensemble of the separation bubble and the shock system is subjected to unsteady motions that spread on a wide range of characteristic frequencies. For instance, an oscillatory behavior of the reflected shock has been observed for high-frequency ranges [12], representative of the most energetic turbulent scales of the incoming boundary layers. Kelvin-Helmholtz waves are also depicted, destabilizing the occurring shear layer and leading to vortex shedding. Another oscillatory motion is the so-called bubble “breathing,” a low-frequency instability corresponding to enlargement and shrinkage of the bubble, observed both numerically and experimentally [1]. Studies on the topic are numerous [13–15], although no clear consensus on the specific source of this flow unsteadiness (e.g., upstream boundary layer fluctuations, shear layer entertainment mechanism, intermittency) has been found yet. Several parameters can affect the overall SWBLI dynamics, among which it is noteworthy mentioning the effect of nonadiabatic walls. It has been found that wall cooling tends to reduce the interaction scales and the bubble size while increasing pressure fluctuations [16,17].

More recently, attention has been paid to shock-wave/transitional boundary layer interactions [18–22]. These studies are meant to mimic more realistic configurations in which the boundary layer is not completely unperturbed, but may be subjected to random disturbances deriving from the external flow or naturally generated in wind tunnel facilities.

Of particular interest is the high-enthalpy hypersonic regime (encountered in reentry and low-altitude hypersonic flight problems), in which the assumption of calorically perfect gas is no longer valid and out-of-equilibrium processes can be triggered at the high temperatures induced by the intense wall friction and the strong shock waves. In such configurations, chemical dissociation and vibrational relaxation phenomena interplay with the SWBLI physics. High-enthalpy effects on turbulent flows have gained renewed attention for smooth boundary layer configurations [23–27], where their influence was often found to be important depending on the thermodynamic operating regime. On the other hand, most of the research on shock-wave boundary layer interactions is limited to calorically perfect gas assumptions and low-enthalpy conditions. To the authors’ knowledge, the presence of high-enthalpy effects in SWBLI has been considered by only Volpiani [28] and Passiatore *et al.* [29], with the purpose in both cases of assessing the capabilities of numerical methods in robustly handling such severe configurations.

The main objective of this study is therefore twofold: (1) to extend the knowledge of high-enthalpy wall-bounded turbulent flows to configurations involving the impingement of shock waves and (2) to produce high-fidelity data to be exploited for the calibration and validation of turbulence models for high-enthalpy flows, which until now have been limited to simple zero-pressure-gradient boundary layer configurations. For that purpose, we perform a direct numerical simulation (DNS) of a shock-wave/hypersonic boundary layer interaction in the presence of both chemical and thermal nonequilibrium effects. The boundary layer considered in this work is excited by means of superimposed freestream disturbances and is found to be in a transitional state at the location of shock impingement. The selected thermodynamic conditions are such that the timescales of the flow and those of the vibrational relaxation processes are comparable, resulting in a regime of strong thermal nonequilibrium.

The paper is organized as follows. Section II describes the governing equations and the thermochemical models used for the computation. The numerical strategy adopted and the problem setup are reported in Secs. III and IV, respectively. Section V presents the main results, providing a general overview of the flow dynamics, particular insights on the interaction region, inspections on turbulent statistics, and a detailed analysis of the thermochemical flow field. Concluding remarks are provided in Sec. V.

II. GOVERNING EQUATIONS

The fluid under investigation is air at high temperature in thermochemical nonequilibrium, modeled as a five-species mixture of N_2, O_2, NO, O, and N. Such flows are therefore governed by the compressible Navier-Stokes equations for multicomponent chemically reacting and thermally relaxing gases, which read

$$\frac{\partial \rho}{\partial t}+\frac{\partial \rho u_j}{\partial x_j}=0, \tag{1}$$

$$\frac{\partial \rho u_i}{\partial t}+\frac{\partial(\rho u_i u_j+p\delta_{ij})}{\partial x_j}=\frac{\partial \tau_{ij}}{\partial x_j}, \tag{2}$$

$$\frac{\partial \rho E}{\partial t}+\frac{\partial[(\rho E+p)u_j]}{\partial x_j}=\frac{\partial(u_i\tau_{ij})}{\partial x_j}-\frac{\partial\left(q_j^{\mathrm{TR}}+q_j^{\mathrm{V}}\right)}{\partial x_j}-\frac{\partial}{\partial x_j}\left(\sum_{n=1}^{\mathrm{NS}}\rho_n u_{nj}^D h_n\right), \tag{3}$$

$$\frac{\partial \rho_n}{\partial t}+\frac{\partial(\rho_n u_j)}{\partial x_j}=-\frac{\partial \rho_n u_{nj}^D}{\partial x_j}+\dot{\omega}_n \qquad (n=1,\dots,\mathrm{NS}-1), \tag{4}$$

$$\frac{\partial \rho e_{\mathrm{V}}}{\partial t}+\frac{\partial \rho e_{\mathrm{V}} u_j}{\partial x_j}=\frac{\partial}{\partial x_j}\left(-q_j^{\mathrm{V}}-\sum_{m=1}^{\mathrm{NM}}\rho_m u_{mj}^D e_{\mathrm{V}m}\right)+\sum_{m=1}^{\mathrm{NM}}(Q_{\mathrm{TV}m}+\dot{\omega}_m e_{\mathrm{V}m}). \tag{5}$$

In the preceding formulation, ρ is the mixture density, t the time coordinate, x_j the space coordinate in the jth direction of a Cartesian coordinate system, with u_j the velocity vector component in the same direction, p the pressure, δ_{ij} the Kronecker symbol, and τ_{ij} the viscous stress tensor, modeled as

$$\tau_{ij}=\mu\left(\frac{\partial u_i}{\partial x_j}+\frac{\partial u_j}{\partial x_i}\right)-\frac{2}{3}\mu\frac{\partial u_k}{\partial x_k}\delta_{ij}, \tag{6}$$

with μ the mixture dynamic viscosity. In Eq. (3), $E=e+\frac{1}{2}u_i u_i$ is the specific total energy (with e the mixture internal energy), and q_j^{TR} and q_j^{V} the rotranslational and vibrational contributions to the heat flux, respectively; u_{nj}^D denotes the diffusion velocity and h_n the specific enthalpy for the nth species. In the species conservation equations (4), $\rho_n=\rho Y_n$ represents the nth species partial density (Y_n being the mass fraction) and $\dot{\omega}_n$ the rate of production of the nth species. The sum of the partial densities is equal to the mixture density $\rho=\sum_{n=1}^{\mathrm{NS}}\rho_n$, NS being the total number of species. To ensure total mass conservation, the mixture density and $\mathrm{NS}-1$ species conservation equations are solved, while the density of the NSth species is computed as $\rho_{\mathrm{NS}}=\rho-\sum_{n=1}^{\mathrm{NS}-1}\rho_n$. We set such species with molecular nitrogen being the most abundant one throughout the computational domain. As for Eq. (5), $e_{\mathrm{V}} = \sum_{m=1}^{\mathrm{NM}} Y_m e_{\mathrm{V}m}$ represents the mixture vibrational energy, with $e_{\mathrm{V}m}$ the vibrational energy of the mth molecule and NM their total number. In the same equation, $Q_{\mathrm{TV}} = \sum_{m=1}^{\mathrm{NM}} Q_{\mathrm{TV}m}$ represents the energy exchange between vibrational and translational modes (due to molecular collisions and linked to energy relaxation phenomena) and $\sum_{m=1}^{\mathrm{NM}} \dot{\omega}_m e_{\mathrm{V}m}$ the vibrational energy lost or gained due to molecular depletion or production. Each species is assumed to behave as a thermally perfect gas; Dalton's pressure mixing law leads to the thermal equation of state:

$$p = \rho T \sum_{n=1}^{\mathrm{NS}} \frac{\mathcal{R} Y_n}{\mathcal{M}_n} = T \sum_{n=1}^{\mathrm{NS}} \rho_n R_n, \tag{7}$$

R_n and $\mathcal{M}_n$ being the gas constant and molecular weight of the nth species, respectively, and $\mathcal{R} = 8.314\,\mathrm{J/mol\,K}$ the universal gas constant. The thermodynamic properties of high-T air species are computed considering the contributions of translational, rotational, and vibrational modes; specifically, the rigid rotor and harmonic oscillator thermal model is used. In this approach, the internal energy reads

$$e = \sum_{n=1}^{\mathrm{NS}} Y_n h_n - \frac{p}{\rho}, \quad \text{with} \quad h_n = h_{f,n}^0 + \int_{T_{\mathrm{ref}}}^{T} \left(c_{p,n}^{\mathrm{T}} + c_{p,n}^{\mathrm{R}}\right) dT' + e_{\mathrm{V}n}(T_{\mathrm{V}}). \tag{8}$$

Here $h_{f,n}^0$ is the nth species enthalpy of formation at the reference temperature ($T_{\mathrm{ref}} = 298.15\,\mathrm{K}$), $c_{p,n}^{\mathrm{T}}$ and $c_{p,n}^{\mathrm{R}}$ the translational and rotational contributions to the isobaric heat capacity of the nth species, computed as

$$c_{p,n}^{\mathrm{T}} = \frac{5}{2} R_n \qquad \text{and} \qquad c_{p,n}^{\mathrm{R}} = \begin{cases} R_n & \text{for diatomic species} \\ 0 & \text{for monoatomic species} \end{cases}, \tag{9}$$

and $e_{\mathrm{V}n}$ the vibrational energy of species n, given by

$$e_{\mathrm{V}n} = \frac{T_{V,n}^{\star} R_n}{\exp\left(T_{V,n}^{\star}/T_{\mathrm{V}}\right) - 1}, \tag{10}$$

with $T_{V,n}^{\star}$ the characteristic vibrational temperature of each molecule (3393 K, 2273 K, and 2739 K for N_2, O_2, and NO, respectively). After the numerical integration of the conservation equations, the rotranslational temperature T is computed from the specific internal energy (devoid of the vibrational contribution) directly, whereas an iterative Newton-Raphson method is used to compute T_{V} from $e_{\mathrm{V}} = \sum_{m=1}^{\mathrm{NM}} Y_m e_{\mathrm{V}m}$.

Both heat fluxes are modeled by means of Fourier's law, $q_j^{\mathrm{TR}} = -\lambda_{\mathrm{TR}} \frac{\partial T}{\partial x_j}$ and $q_j^{\mathrm{V}} = -\lambda_{\mathrm{V}} \frac{\partial T_{\mathrm{V}}}{\partial x_j}$, λ_{TR} and λ_{V} being the rotranslational and vibrational thermal conductivities, respectively. To close the system, we use the two-temperature model of Park [30] to take into account the simultaneous presence of thermal and chemical nonequilibrium for the computation of $\dot{\omega}_n$ and Q_{TV}. Specifically, the five species interact with each other through a reaction mechanism consisting of five reversible chemical steps [31]:

$$\begin{aligned}
&\text{R1:} && \mathrm{N_2 + M} \Longleftrightarrow \mathrm{2N + M}, \\
&\text{R2:} && \mathrm{O_2 + M} \Longleftrightarrow \mathrm{2O + M}, \\
&\text{R3:} && \mathrm{NO + M} \Longleftrightarrow \mathrm{N + O + M}, \\
&\text{R4:} && \mathrm{N_2 + O} \Longleftrightarrow \mathrm{NO + N}, \\
&\text{R5:} && \mathrm{NO + O} \Longleftrightarrow \mathrm{N + O_2},
\end{aligned} \tag{11}$$

where M is the third body (any of the five species considered). Dissociation and recombination processes are described by reactions R1, R2, and R3, whereas the shuffle reactions R4 and R5 represent rearrangement processes. The mass rate of production of the nth species is governed by the law of mass action:

$$\dot{\omega}_n = \mathcal{M}_n \sum_{r=1}^{\mathrm{NR}} (\nu''_{nr} - \nu'_{nr}) \times \left[k_{f,r} \prod_{n=1}^{\mathrm{NS}} \left(\frac{\rho Y_n}{\mathcal{M}_n} \right)^{\nu'_{nr}} - k_{b,r} \prod_{n=1}^{\mathrm{NS}} \left(\frac{\rho Y_n}{\mathcal{M}_n} \right)^{\nu''_{nr}} \right], \tag{12}$$

where ν'_{nr} and ν''_{nr} are the stoichiometric coefficients for reactants and products in the rth reaction for the nth species, respectively, and NR is the total number of reactions. Furthermore, $k_{f,r}$ and $k_{b,r}$ denote the forward and backward rates of the rth reaction, modeled by means of Arrhenius' law. Additional details about their computation can be found in [26]. The coupling between chemical and thermal nonequilibrium is taken into account by means of a modification of the temperature values used for computing the reaction rates. Indeed, a geometric-averaged temperature is considered for the dissociation reactions R1, R2, and R3 in (11), computed as $T_{\mathrm{avg}} = T^q T_{\mathrm{V}}^{1-q}$ with $q = 0.7$ [30].

Last, the vibrational-translational energy exchange is computed as

$$Q_{\mathrm{TV}} = \sum_{m=1}^{\mathrm{NM}} Q_{\mathrm{TV},m} = \sum_{m=1}^{\mathrm{NM}} \rho_m \frac{e_{\mathrm{V}m}(T) - e_{\mathrm{V}m}(T_{\mathrm{V}})}{t_m}, \tag{13}$$

where t_m is the corresponding relaxation time evaluated by means of the expression [32]

$$t_m = \sum_{n=1}^{\mathrm{NS}} \frac{\rho_n}{\mathcal{M}_n} \sum_{n=1}^{\mathrm{NS}} \frac{t_{mn}}{\rho_n/\mathcal{M}_n}. \tag{14}$$

Here t_{mn} is the relaxation time of the mth molecule with respect to the nth species, computed as the sum of two contributions

$$t_{mn} = t_{mn}^{MW} + t_{mn}^{c}. \tag{15}$$

The first term is written

$$t_{mn}^{\mathrm{MW}} = \frac{p}{p_{\mathrm{atm}}} \exp\left[a_{mn}\left(T^{-\frac{1}{3}} - b_{mn}\right) - 18.42 \right], \tag{16}$$

where $p_{\mathrm{atm}} = 101325\,\mathrm{Pa}$ and a_{mn} and b_{mn} are coefficients reported in [33]. Since this expression tends to underestimate the experimental data at temperatures above 5000 K, a high-temperature correction was proposed by Park [34],

$$t_{mn}^{c} = \sqrt{\frac{\phi_{mn}}{\mathcal{M}_m \sigma}}, \tag{17}$$

where $\phi_{mn} = \frac{\mathcal{M}_m \mathcal{M}_n}{\mathcal{M}_m + \mathcal{M}_n}$ and $\sigma = \sqrt{\frac{8\mathcal{R}}{T\pi}} \frac{7.5\times10^{-12}\mathrm{NA}}{T}$, NA being Avogadro's number. Note that this correction is taken into account in our numerical simulations, although such high temperatures are hardly reached in the computational domain under the thermodynamic conditions currently investigated.

As for the computation of the transport properties, pure species' viscosity and thermal conductivities are computed using curve fits by Blottner [35] and Eucken's relations [36], respectively. The corresponding mixture properties are evaluated by means of Wilke's mixing rules [37]. Mass diffusion is modeled by means of Fick's law:

$$\rho_n u_{nj}^{D} = -\rho D_n \left(\frac{\partial Y_n}{\partial x_j} + Y_n \frac{\partial \ln \mathcal{M}}{\partial x_j} \right) + \rho_n \sum_{n=1}^{\mathrm{NS}} D_n \left(\frac{\partial Y_n}{\partial x_j} + Y_n \frac{\partial \ln \mathcal{M}}{\partial x_j} \right), \tag{18}$$

where $\mathcal{M}$ is the mixture molecular weight. Here the first term on the r.h.s. represents the effective diffusion velocity, and the second one is a mass corrector term that should be taken into account in order to satisfy the continuity equation when dealing with nonconstant species diffusion coefficients

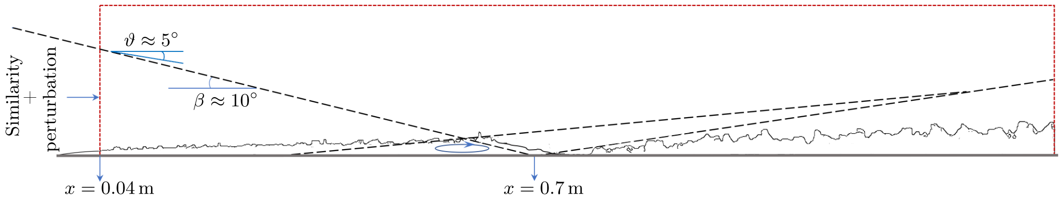

FIG. 1. Sketch of the configuration under investigation.

[38]. Specifically, D_n is an equivalent diffusion coefficient of species n into the mixture, computed following Hirschfelder's approximation [36], starting from the binary diffusion coefficients which are curve fitted in [39].

III. NUMERICAL METHODOLOGY

The numerical solver described in Sciacovelli *et al.* [40] is used for the present computation. The Navier-Stokes equations are integrated numerically by using a high-order finite-difference scheme. The convective fluxes are discretized by means of central tenth-order differences, supplemented with a high-order adaptive nonlinear artificial dissipation. The latter consists in a blend of a ninth-order-accurate dissipation term based on tenth-order derivatives of the conservative variables, used to damp grid-to-grid oscillations, along with a low-order shock-capturing term. This term is equipped with a highly selective pressure-based sensor. For the vibrational energy equation, a sensor based on second-order derivatives of the vibrational temperature is used. Time integration is carried out using a low-storage third-order Runge-Kutta scheme. The numerical strategy has been validated for thermochemical nonequilibrium flows, including SWBLI laminar configurations [29].

IV. PROBLEM SETUP

The configuration under investigation, displayed in Fig. 1, consists in a shock wave that impinges on a thermally and chemically out-of-equilibrium flat-plate boundary layer. We note in the following with ϑ and β the deflection angle and the shock angle, respectively. The current setup stems from the one of Sandham *et al.* [19], in which inflow freestream perturbations were applied on a $M_\infty = 6$ laminar perfect-gas boundary layer; the original case is presented in the Appendix for validation purposes. Here we consider the postshock (PS) conditions of a scramjet, approximated by a 6° planar wedge, flying at Mach 12 at an altitude of 36 km. The freestream conditions are then $T_\infty = 405\,\mathrm{K}$, $p_\infty = 2258.6\,\mathrm{Pa}$, and $M_\infty = 9$, corresponding to a stagnation enthalpy of $H^0_\infty = 6.86\,\mathrm{MJ/kg}$. To deal with calorically imperfect gas mixtures, the generalized Rankine-Hugoniot relations for an arbitrary equation of state are iteratively solved to obtain PS conditions. For the selected freestream Mach number and a shock angle of $\beta = 10^\circ$, the relations give $\vartheta \approx 5^\circ$ and the PS variables $T_{\mathrm{PS}} = 554\,\mathrm{K}$, $p_{\mathrm{PS}} = 6235\,\mathrm{Pa}$, $u_{\mathrm{PS}} = 3620\,\mathrm{m/s}$. These conditions are imposed at the left boundary of the rectangular domain as a jump on the inlet profiles. The inflow plane of the computational domain and the ideal impingement station are located at $x_0 = 0.04\,\mathrm{m}$ and $x_{\mathrm{sh}} = 0.7\,\mathrm{m}$ from the leading edge, respectively. The wall temperature is fixed equal to $T_w = 2500\,\mathrm{K}$ for both the rotranslational and vibrational temperature, and noncatalytic conditions are applied. The inflow profiles are obtained by solving the locally self-similar equations reported in [40], extended to thermochemical nonequilibrium. It is noteworthy to mention that, even if the flow is assumed to be thermally equilibrated at the wall and in the free-stream, strong nonequilibrium conditions develop inside the self-similar boundary layer at such conditions and streamwise location, with a maximum difference of $\Delta T = T - T_V \approx 1100\,\mathrm{K}$ [29]. Characteristic outflow boundary conditions are imposed at the top and right boundaries, whereas periodicity is enforced in the spanwise direction. The extent of the computational domain is $(L_x \times L_y \times L_z)/\delta^\star_{\mathrm{in}} = 800 \times 80 \times 60$, $\delta^\star_{\mathrm{in}} = 1.77 \times 10^{-3}\,\mathrm{m}$ being the displacement thickness at the inlet, defined in Eq. (20). As for the discretization, a total

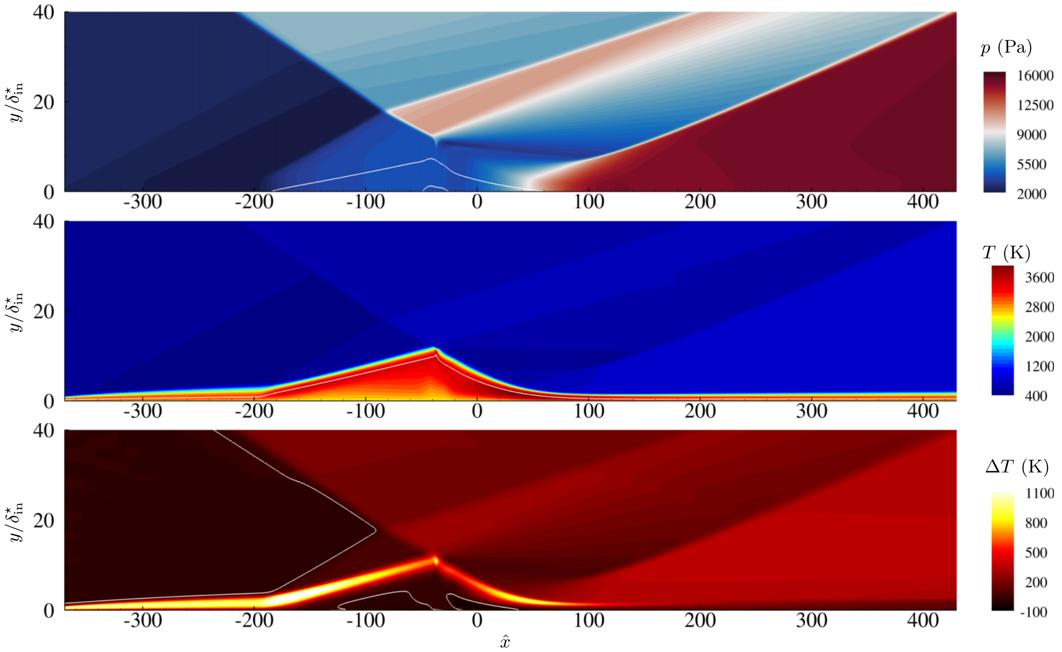

FIG. 2. Visualization of the base flow without perturbation. Top: isocontours of pressure, p; the white lines denote the extent of the recirculation bubble ($u = 0$ isolines). Center: isocontour of rotraslational temperature, T; the white line denotes the sonic line ($M = 1$ isoline). Bottom: isocontours of the temperature difference, $\Delta T = T - T_V$; the white lines denote the $\Delta T = 0$ contour. The y axis has been stretched for better visualization.

number of $N_x \times N_y \times N_z = 6528 \times 402 \times 720$ grid points is used, with constant grid size in the streamwise and spanwise directions and a constant grid stretching of 1% in the wall-normal direction, the height of the first cell away from the wall being $\Delta y_w = 2.5 \times 10^{-5}$ m. Unless otherwise stated, in the following we will make use of a dimensionless streamwise coordinate computed as $\hat{x} = (x - x_{\rm sh})/\delta^\star_{\rm in}$. Figure 2 reports the pressure, rotraslational temperature, and temperature difference ($\Delta T = T - T_V$) isocontours of the base flow used to initialize the three-dimensional computation. The adverse pressure gradient induced by the incident shock generates a recirculation bubble, marked with a white line in the top figure. Upstream of the separation bubble, a series of compression waves occur, which then coalesce into the separation shock; the latter interacts with the incident shock that penetrates the separated flow. Downstream of the separation bubble, a reattachment shock is generated which readjusts the previously deflected flow. Accordingly, the behavior of the rotranslational temperature exhibits the same pattern in the undisturbed flow; a large increase of temperature is encountered in the recirculation region close to the boundary layer edge. Globally, the characteristic features of SWBLI are not altered by high-enthalpy effects; on the other hand, such a complex dynamics strongly influences the thermochemical activity. Coherently with the inlet temperature profiles, the amount of thermal nonequilibrium before the bubble is extremely high while chemical activity is essentially negligible. The rise of the temperatures and pressure in the separation zone enhances chemical dissociation whereas the gap between the two temperatures is reduced, moving towards a quasithermally equilibrated state right after the recirculation bubble. The $\Delta T = 0$ isoline, dividing the thermally under- and overexcited regions, shows that the flow is underexcited everywhere except for the freestream preshock region and in the recirculation bubble, where a slight vibrational overexcitation is observed. A comparison of the configurations with and without shock impingement reveals that, in the latter case, the flow remains in a state of stronger

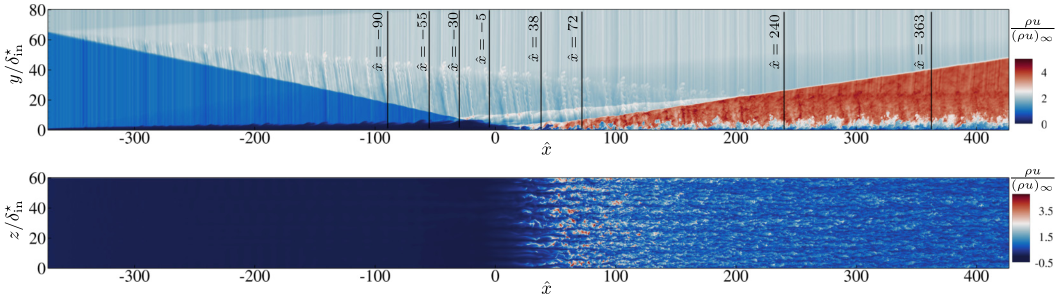

FIG. 3. Instantaneous visualizations of streamwise momentum in a xy plane (top) and in a xz plane at $y/\delta^\star_{\text{in}} = 0.5$ (bottom). The y axis has been stretched for better visualization.

thermal nonequilibrium and quasifrozen chemical activity throughout the entire boundary layer. Therefore, the pressure rise caused by the incident shock is responsible for a reduction of the amount of thermal nonequilibrium and an increase of the chemical activity. Additional details about the base flow can be found in Passiatore *et al.* [29].

Laminar-to-turbulent transition for the three dimensional simulation is favored by superimposing disturbances on the described base flow. Following [19], the density self-similar profile is perturbed as follows:

$$\frac{\rho'}{\rho_\infty} = aW\left(\frac{y}{\delta^\star_{\text{in}}}\right)\sum_{j=1}^{N_J}\cos\left(\frac{2\pi jz}{L_z} + \Phi_j\right)\sum_{k=1}^{N_K}\sin\left(2\pi \hat{f}_k\frac{u_\infty}{\delta^\star_{\text{in}}}t + \Psi_k\right), \tag{19}$$

Here $W(y/\delta^\star_{\text{in}}) = 1 - \exp[-(y/\delta^\star_{\text{in}})^3]$ is a function that damps the disturbances near the wall, and Φ_j and Ψ_k are the phases that correspond to random numbers between 0 and 2π, with $N_J = 16$ and $N_K = 20$. The dimensionless frequency $\hat{f}_k$ is set equal to $0.02k$, whereas the amplitude of the perturbation is $a = 5 \times 10^{-4}$. It should be noted that the latter value is rather high and can be considered as being representative of wind tunnel test conditions more than actual flight conditions. Although its precise value is likely to influence the location of the transition point (which moves downstream for lower amplitudes), the flow dynamics of the interaction region is expected to be only mildly affected.

V. RESULTS

In the results presented below, flow statistics are computed by averaging in time and in the spanwise homogeneous direction, and after that the initial transient has been evacuated. For a given variable f, we denote with $\overline{f} = f - f'$ the standard time- and spanwise average, f' being the corresponding fluctuation, whereas $\widetilde{f} = f - f'' = \overline{\rho f}/\overline{\rho}$ denotes the density-weighted Favre averaging, with f'' the Favre fluctuation. Statistics are collected for a period corresponding to $T_{\text{stats}} \approx 2050\delta^\star_{\text{in}}/u_\infty$, for a total of approximately 40 000 temporal snapshots. The sampling frequency is approximately 1000 and 60 times larger than the lowest and the highest harmonic in the perturbation function, respectively (i.e., $\Delta t_{\text{stats}} \approx 4.38 \times 10^{-2}\delta^\star_{\text{in}}/u_\infty$).

Profiles of various dynamic, thermodynamic, and thermochemical flow quantities are extracted at eight stations in the laminar region, before the shock impingement, in the interaction zone and in the fully turbulent state. The location of such stations is marked in Fig. 3, displaying the isocontours of the streamwise momentum in a xy slice (top) and a near-wall xz slice (bottom). In the top panel, a shock pattern similar to the one in the base flow of Fig. 2 can be appreciated, as well as the presence of the superimposed density disturbances in the free-stream. Due to the thickening of the perturbed boundary layer upstream of the impingement, it is possible to detect a distinguishable separation shock only after the interaction with the incident one. The angulation of

TABLE I. Boundary layer properties at eight selected streamwise stations. $\mathrm{Re}_x = \rho_\infty u_\infty x/\mu_\infty$ is the Reynolds number based on the distance from the leading edge, $\mathrm{Re}_\tau = \overline{\rho}_w u_\tau \delta/\overline{\mu}_w$ is the friction Reynolds number, $\mathrm{Re}_\theta = \rho_\infty u_\infty \theta/\mu_\infty$ and $\mathrm{Re}_{\theta,i} = \mu_\infty/\overline{\mu}_w \mathrm{Re}_\theta = \rho_\infty u_\infty \theta/\mu_w$ are the Reynolds numbers based on local momentum thickness and its incompressible-transformed counterpart [41], respectively, $\mathrm{Re}_{\delta^\star} = \rho_\infty u_\infty \delta^\star/\mu_\infty$ is the Reynolds number based on the displacement thickness, and H is the shape factor. Δx^+, Δy_w^+, and Δz^+ denote the grid sizes in inner variables in the x direction, y direction at the wall, and the z direction, respectively.

	Legend	$\hat{x}$	$10^{-5}\mathrm{Re}_x$	Re_τ	Re_θ	$\mathrm{Re}_{\theta,i}$	$10^{-3}\mathrm{Re}_{\delta^\star}$	H	Δx^+	Δz^+	Δy_w^+
Laminar	-·-·-	-90	16.43	–	864.1	261.7	20.64	23.9	–	–	–
Separation	-·-·-	-55	18.57	–	984.6	298.3	23.55	23.9	–	–	–
Inside bubble	-·-·-	-30	19.74	–	1003	303.8	29.32	29.2	–	–	–
Reattachment	-·-·-	-5	21.17	–	962.6	292.4	19.24	20.0	–	–	–
Transition	-·-·-	38	23.41	245.6	1170	354.1	8.942	7.64	8.87	6.02	1.02
Transition	-·-·-	72	25.21	392.5	1108	335.4	7.755	7.00	7.43	5.05	0.86
Turbulent	-·-·-	240	34.29	517.9	1520	460.4	13.69	9.00	8.89	6.04	1.02
Turbulent	-·-·-	363	40.90	562.4	1957	594.6	16.86	8.61	8.76	5.96	1.00

the separation shock is such that it impacts the reattachment shock, differently from the base flow. Table I reports some boundary layer properties at the selected positions. Throughout the paper, the superscript "$\bullet^+$" denotes normalization with respect to the viscous length scale $\ell_v = \overline{\mu}_w/(\overline{\rho}_w u_\tau)$, $u_\tau = \sqrt{\overline{\tau}_w/\overline{\rho}_w}$ being the wall friction velocity. The boundary layer displacement thickness, the momentum thickness and the shape factor are defined as

$$\delta^\star = \int_0^\delta \left(1 - \frac{\rho u}{\rho_\delta u_\delta}\right) dy, \qquad \theta = \int_0^\delta \frac{\rho u}{\rho_\delta u_\delta}\left(1 - \frac{u}{u_\delta}\right) dy, \qquad H = \frac{\delta^\star}{\theta}, \tag{20}$$

where the subscript δ denotes the variables computed at the edge of the boundary layer. Mesh spacing in wall units, reported in the table, shows that DNS-like resolution is achieved throughout the domain. The wall-normal profiles of statistics are mostly displayed in inner semilocal units $y^\star = \overline{\rho} u_\tau^\star y/\overline{\mu}$, with $u_\tau^\star = \sqrt{\overline{\tau}_w/\overline{\rho}}$, or in outer scaling y/δ.

A. Overview of flow dynamics

Figure 4 shows a three-dimensional view of the flow structures for an instantaneous snapshot. Traces of the inflow perturbation are visible in the free-stream after the impinging shock. The disturbances interact with the incoming laminar boundary layer and destabilize it, leading to the generation of coherent structures upstream of the interaction region. Two-dimensional near-wall

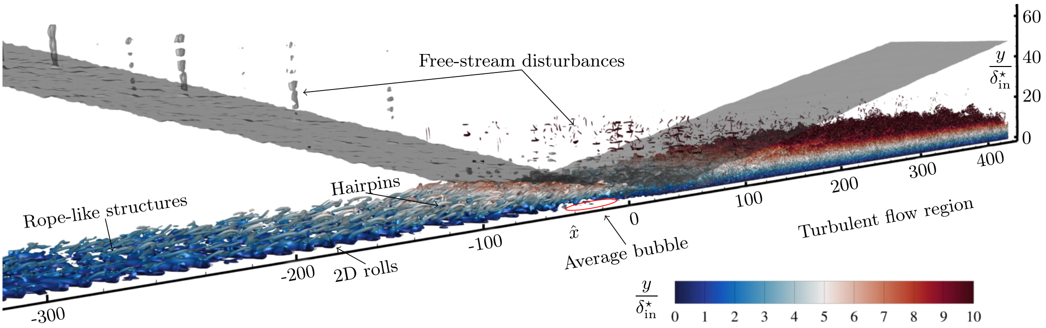

FIG. 4. Isosurfaces of the Q criterion colored with the wall distance for an instantaneous snapshot. The red circle denotes the location of the average recirculation bubble.

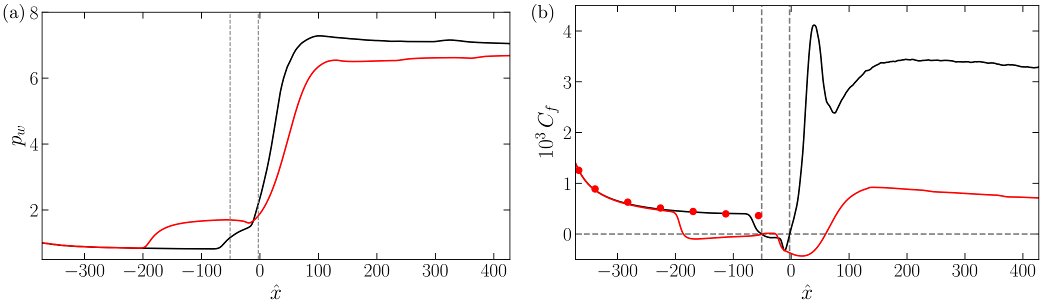

FIG. 5. Evolution of normalized wall pressure p_w (a) and skin friction coefficient (b). Red lines represent the evolution of the same quantities in the base flow computation; vertical lines stand for the beginning and the end of the separation zone in the 3D computation, whereas the horizontal line in panel (b) denotes the $C_f = 0$ isoline. Symbols in panel (b) mark the results of the locally self-similar theory.

rolls are visible beneath ropelike structures; the latter evolve giving rise to hairpins ahead of the recirculation region that break down at the interaction. Despite the rich variety of flow structures populating the boundary layer, the analysis of wall quantities reveal that it essentially follows a laminar-like evolution almost up to the average separation point, as will be shown later. We start the analysis with the streamwise distributions of the normalized wall pressure $p_w = \overline{p}/p_\infty$ and the skin friction coefficient $C_f = \frac{2\overline{\tau}_w}{\rho_\infty u_\infty^2}$, reported in Figs. 5(a) and 5(b), respectively. The vertical lines represent the beginning and the end of the separation zone, computed by intersecting the $C_f = 0$ isoline with the evolution of the statistically averaged skin friction coefficient. In the same figures, the laminar base flow solution is reported with red lines. In the laminar case, the pressure jump across the interaction zone is ≈6, whereas it reaches ≈7 in the three-dimensional transitional case. As already observed by Sandham *et al.* [19] for cold SWBLI at $M_\infty = 6$, there is a significant reduction of the bubble length with respect to the laminar case, the separation region L_{sep} being equal to $48\delta^\star_{\text{in}}$. The behavior may be attributed to the freestream perturbation causing a reduction of the shock strength, but also to the different nature of the incoming boundary layer which causes increased mixing due to velocity fluctuations [see, e.g., 42]. Of particular interest is the different trend of the skin friction coefficient with respect to the base flow, even before the shock impingement. In the region $-200 < \hat{x} < -80$, the C_f follows the laminar distributions, deviating from the base flow profile for which the recirculation zone begins at $\hat{x} \approx -200$. Of note, the evolution in the upstream zone is in perfect agreement with the results estimated by the locally self-similar theory [represented by the red dots in Fig. 5(b)]. In the fully turbulent region downstream of the interaction, C_f values are approximately four times larger than those registered in the laminar case, similarly to [19]. On the other hand, its evolution in the interaction region is rather different. The increase observed after reaching the global minimum, at $\hat{x} \approx 0$, is attributed to the reattachment. As the C_f experiences a ramplike increase, at $\hat{x} \approx 40$, the incident shock penetrates the boundary layer and reaches the wall, causing a sudden increase of wall friction and heating.

The evolution of the two contributions of the normalized wall heat flux, defined as

$$q_w^{\text{TR}} = \frac{\overline{\lambda_{\text{TR}} \partial T/\partial y}}{\rho_\infty u_\infty^3}, \qquad q_w^{\text{V}} = \frac{\overline{\lambda_{\text{V}} \partial T_V/\partial y}}{\rho_\infty u_\infty^3}, \tag{21}$$

is reported in Figs. 6(a) and 6(b). The results are also compared with the corresponding laminar evolutions of the same quantities. The rotranslational heat flux, q_w^{TR}, follows essentially the C_f distribution, with a minimum in the separation zone, a peak of almost 10^{-4}, and a significant overheating in the fully turbulent region with respect to the case without perturbation. Of particular interest is the trend of the vibrational heat flux. As already observed in the flat-plate boundary layer configuration investigated by Passiatore *et al.* [26], the latter is one order of magnitude smaller

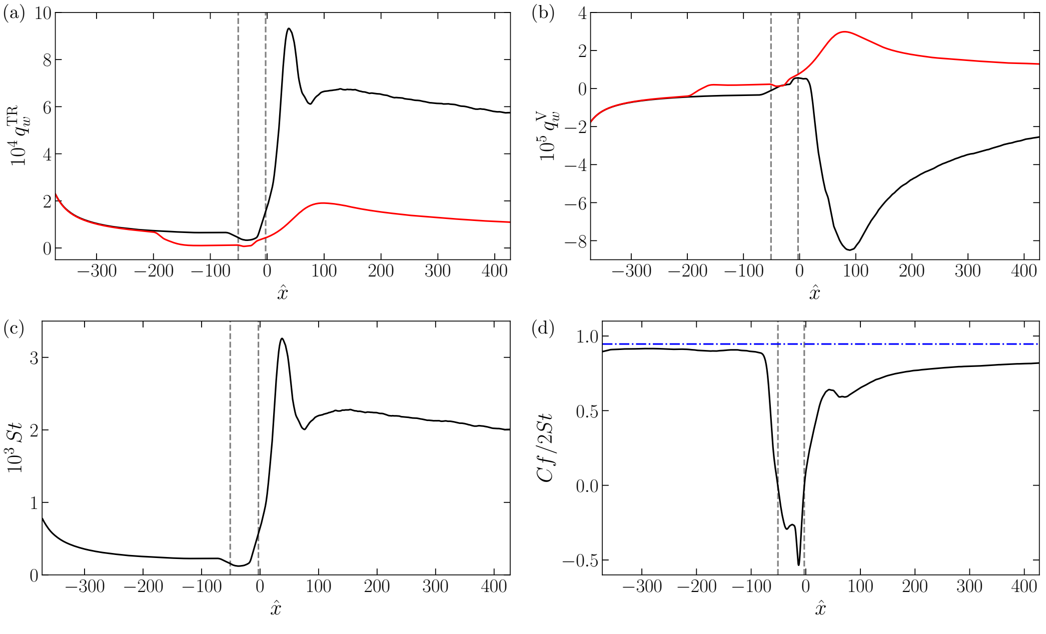

FIG. 6. Top: distribution of the translational-rotational contribution (a) and the vibrational contribution (b) of the normalized heat flux at the wall. Red lines denote the base flow evolution of the corresponding variables. Bottom: evolution of the Stanton number (c) and the Reynolds analogy between C_f and St (d). The blue horizontal dashed-dotted line in panel (d) represents the $\mathrm{Pr}^{2/3}$ line.

with respect to the rotranslational one. However, thermal nonequilibrium before the interaction is so strong that the wall heats the flow from a vibrational energy standpoint (i.e., $q_w^{\rm V}$ is negative and the profiles of $T_{\rm V}$ are monotonic, as will be shown in Sec. V D). For the case without perturbation, the vibrational heat flux switches to positive values in the recirculation bubble, then increases in the reattachment region, and relaxes to the PS conditions while keeping positive values. On the other hand, when perturbations are added, $q_w^{\rm V}$ keeps negative values almost everywhere, except in the small separation bubble. From the reattachment region onwards, its streamwise evolution is opposed to the one obtained in the laminar regime. The global increase of temperature due to the shock impingement causes strong aerodynamic heating, transferring a considerable amount of kinetic energy into internal energy, which is distributed across all the energetic modes. In the same figure, we also report the evolution of the total Stanton number, defined as

$$\mathrm{St} = \frac{q_w}{\rho_\infty u_\infty (h_{aw} - h_\infty)}, \tag{22}$$

where $q_w = \overline{\lambda_{\rm TR}\partial T/\partial y} + \overline{\lambda_{\rm V}\partial T_{\rm V}/\partial y}$ and $h_{aw} = h_\infty + \frac{1}{2} r u_\infty^2$, with $r = 0.9$. Note that the recovery factor has the same value previously used for high-enthalpy configurations [23,26]. The evolution of the Stanton number is in accordance with the trend of the translational contribution of the wall heat flux. The orders of magnitude after the breakdown are in accordance with results for calorically perfect gases [16,19] and with high-enthalpy thermally equilibrated boundary layers [23]. Therefore, the small vibrational heat flux contribution does not affect the Stanton number distribution even in the present strong thermochemical nonequilibrium conditions. In Fig. 6(d) we assess the validity of the Reynolds analogy relating C_f and St. The ratio $C_f/(2\mathrm{St})$ is expected to vary as $\mathrm{Pr}^{2/3}$ (with $\mathrm{Pr} = \mu c_p/\lambda$), which amounts to ≈0.85 for classical values of the Prandtl number. In the present case, the mean Prandtl number reaches ≈0.9 in the near-wall region and displays a nearly constant streamwise evolution [as shown in Fig. 6(d)], with variations in the recirculation region less than

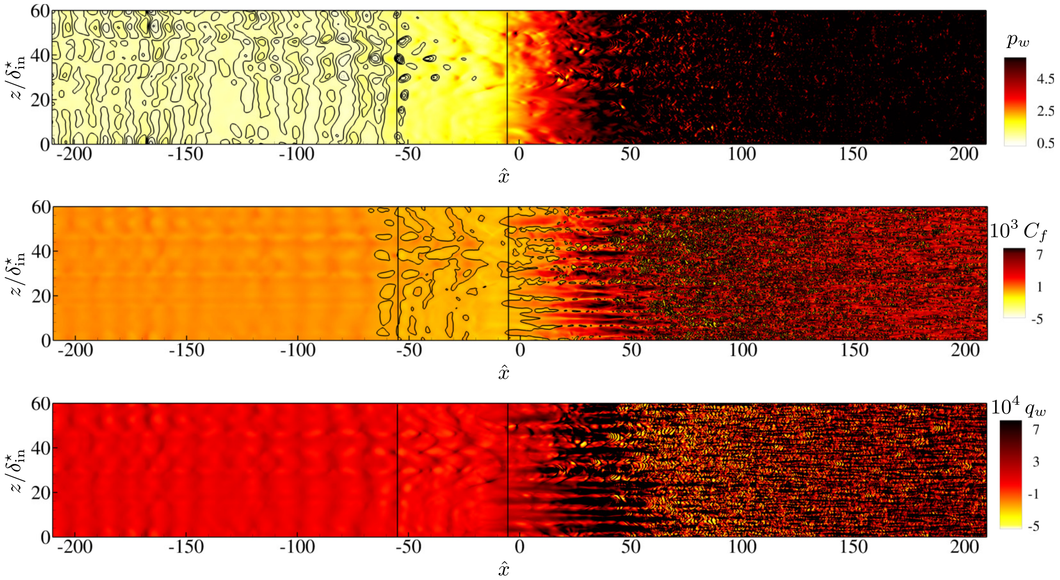

FIG. 7. Top: isocontours of normalized wall pressure p_w and pressure isolines; middle: isocontours of the instantaneous skin friction coefficient C_f, along with $C_f = 0$ isolines; bottom: isocontours of instantaneous normalized total wall heat flux, q_w. The vertical black lines in each panel mark the beginning and the end of the separation bubble.

1% with respect to the turbulent zone. As previously observed for other SWBLI configurations in the literature, the relation performs poorly in the interaction region and seems to slowly relax back to the expected trend afterwards. It is reasonable to suppose that $C_f/(2\text{St})$ tends asymptotically to $\text{Pr}^{2/3}$, although longer computational domains would be needed to confirm its validity [43].

B. Flow field near the interaction

Figure 7 shows instantaneous views of the wall pressure (top), skin friction coefficient (middle), and total wall heat flux (bottom) in the neighborhood of the shock impingement region. The average reversed flow region is also marked with isolines. In the three figures, the footprint of the freestream perturbations is visible in the form of wave packets, corresponding to pressure isolines smaller than p_∞ in the top figure. These wave packets remain coherent up to the separation point and start to destabilize in the bubble at $z/\delta^\star_{\text{in}} \approx 40$, although they do not completely break. After the reattachment point, breakdown to turbulence begins and C_f rapidly increases towards its PS value. For the conditions under investigation, the breakdown is particularly sharp as witnessed by the large overshoot of C_f. This is related to the emergence of energetic structures at $\hat{x} \approx 40$ visible in the middle and bottom panels of Fig. 7. Further downstream, the skin friction reaches a local minimum at $\hat{x} \approx 50$, and the flow relaxes to equilibrium turbulence starting from $\hat{x} \approx 190$. Despite the statistically averaged separation region being small, relatively large structures of negative skin friction coefficient (middle panel of Fig. 7) are visible, showing that instantaneous separation exists well upstream and downstream of the average bubble.

The topology of the separation bubble along an xy plane cut is highlighted in the mean streamwise velocity plot, displayed in the top panel of Fig. 8. In the same figure, the yellow and black lines represent the $\widetilde{u} = 0$ and the sonic line, respectively. The recirculation bubble is found to be very flat and close to the sonic line. The width of the bubble depends on many parameters, such as the shock angle β, the amount of wall cooling, and the Reynolds number at the impinging station; further investigations will be performed in the future to assess the sensitivity of the bubble size to

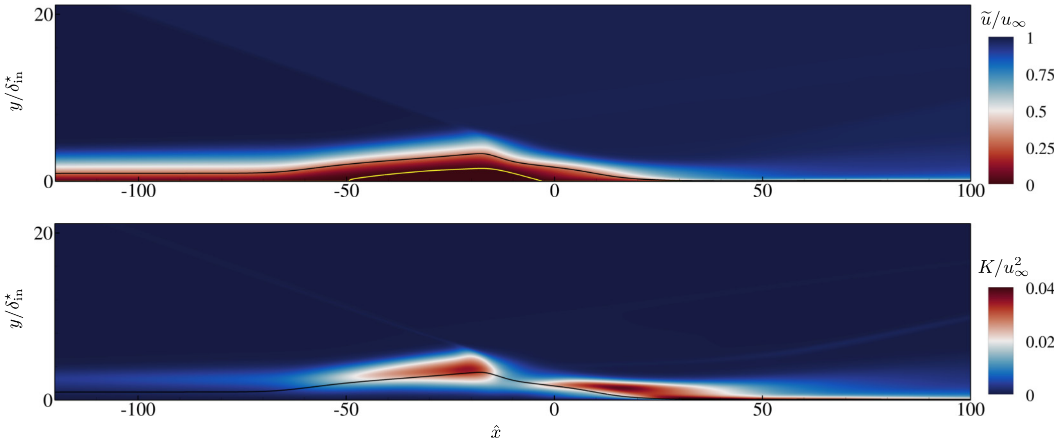

FIG. 8. Visualization of normalized mean streamwise velocity (top panel) and normalized fluctuating kinetic energy (bottom panel).

them. Even if the flow regime in the interaction region is still transitional, another variable worth investigating is the fluctuating kinetic energy $K = \widetilde{u_i''u_i''}/2$. Inspection of Fig. 8 (bottom) illustrates that there are three peaks of kinetic energy emerging in the proximity of the interaction region. The first peak of K, at $\hat{x} \approx -21$, corresponds to the shear layer at the interface with the recirculation bubble, as already pointed out, for instance, by Volpiani *et al.* [17]. The second peak (at $\hat{x} \approx 16$) is shifted towards the wall and comes from the interaction with the reflected shock. The third and last peak, registered at $\hat{x} \approx 35$, is the closest to the wall; it is due to the impact of the shock foot on the wall and coincides with the global maximum of the skin friction coefficient.

1. Instability mechanisms

The strong adverse pressure gradient associated with the incident shock tends to amplify the boundary layer perturbations injected by the inflow disturbances, inducing transition to turbulence. Nevertheless, the stand-alone perturbation has a large influence on the overall flow dynamics, even before the shock impingement station and the recirculation bubble. Figure 9 reports the isocontours of the streamwise velocity perturbation at $y/\delta^\star_{\rm in} \approx 0.5$ (top panel), $y/\delta^\star_{\rm in} \approx 1$ (middle panel), and $y/\delta^\star_{\rm in} \approx 3$ (bottom panel). The emergence of intense streaky structures is visible starting from $\hat{x} \approx -150$. These structures develop with different characteristic dimensions and intensity moving away from the wall; they are disrupted by the shock impingement and disappear in the recirculation bubble. When the flow reattaches, other less-coherent streaky structures appear and finally break down and lead to transition to turbulence. The observed dynamics further confirms that breakdown to turbulence occurs after the reattachment, coherently with the streamwise evolution of the skin friction coefficient. In the attempt to quantify the breakdown, we follow the procedure of Andersson *et al.* [44] for incompressible flows, and we estimate the streaks amplitude as

$$\mathrm{A}_s = \frac{1}{2u_\infty}\left[\max_{y,z}\,(\overline{u} - u_{\rm BF}) - \min_{y,z}\,(\overline{u} - u_{\rm BF})\right], \tag{23}$$

where $u_{\rm BF}$ stays for the velocity of the base flow. Evaluating their amplitude on the current highly compressible nonequilibrium flow is of course made difficult by the fact that quantitative criteria in the literature exist only for incompressible flows; however, the streamwise evolution of streaks amplitude may help understand their role in the transition process. The analysis is performed over 300 three-dimensional subdomains collected in runtime, spanning the extent $-200 \leqslant \hat{x} \leqslant 150$, $0 \leqslant y/\delta^\star_{\rm in} \leqslant 20$, and $0 \leqslant z/\delta^\star_{\rm in} \leqslant 60$. Figure 10 shows the streamwise evolution of A_s, in the region $-200 < \hat{x} < 150$. As already observed from the instantaneous slices, the streak amplitude

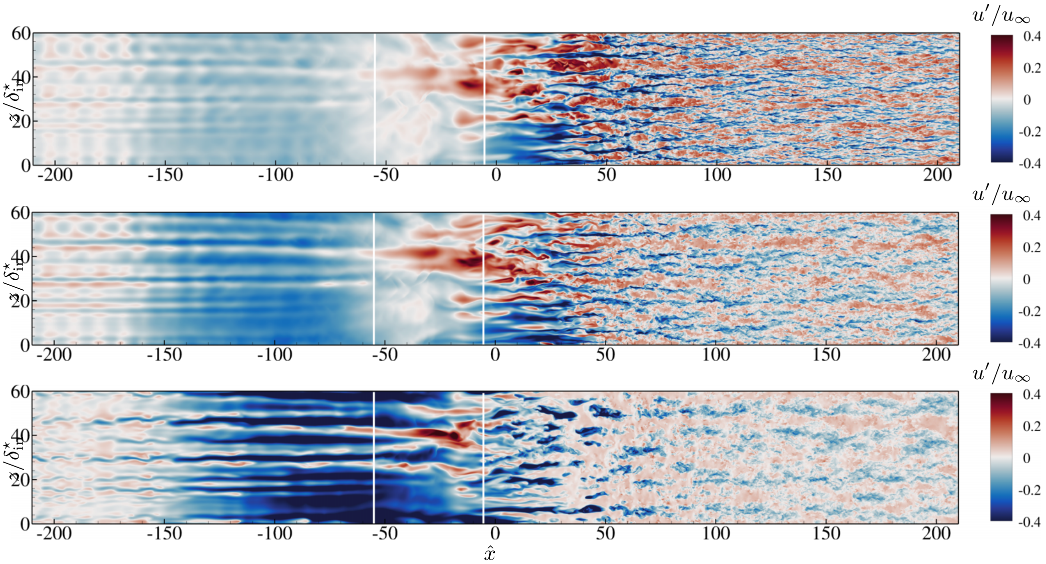

FIG. 9. Isocontours of streamwise velocity perturbation in xz slices, extracted at $y/\delta^\star_{\rm in} = 0.5$ (top), $y/\delta^\star_{\rm in} = 1$ (middle), and $y/\delta^\star_{\rm in} = 3$ (bottom). White vertical lines denote the beginning and the end of the recirculation zone.

grows significantly well upstream of shock impingement, in a region subjected to zero or even a slightly favorable pressure gradient; It is therefore to be uniquely ascribed to the growth of inflow perturbations. Afterwards, the impinging shock disrupts the growing flow structures and generates a recirculation region, which results in a sharp decrease of the estimated streak amplitude. Downstream of $\hat{x} = 0$, the structures grow again up to $\hat{x} \approx 60$, i.e., shortly downstream of the location where the skin friction and the heat flux peak. Then coherence is lost as the flow transitions and the amplitude drop again. Although the previous procedure allows describing the evolution of such stationary structures, the exact transition process is more difficult to detect. The coexistence of the perturbation and the incident shock makes it more difficult to distinguish the different mechanisms that nonlinearly combine to induce breakdown. The instability that often dominates transition in the hypersonic flow regime is the one related to the second (or Mack) mode. This two-dimensional inviscid instability arises when a region of the mean flow becomes supersonic

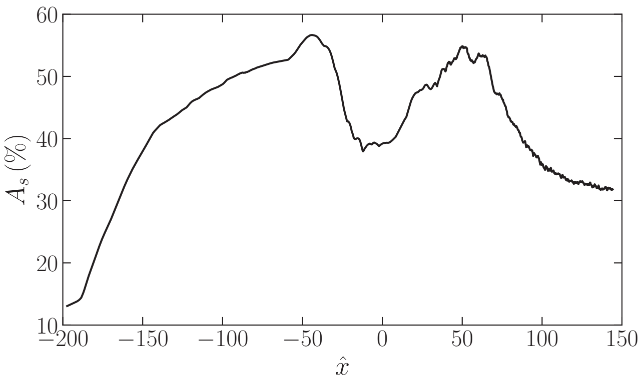

FIG. 10. Streamwise evolution of streaks amplitude, computed as in Eq. (23).

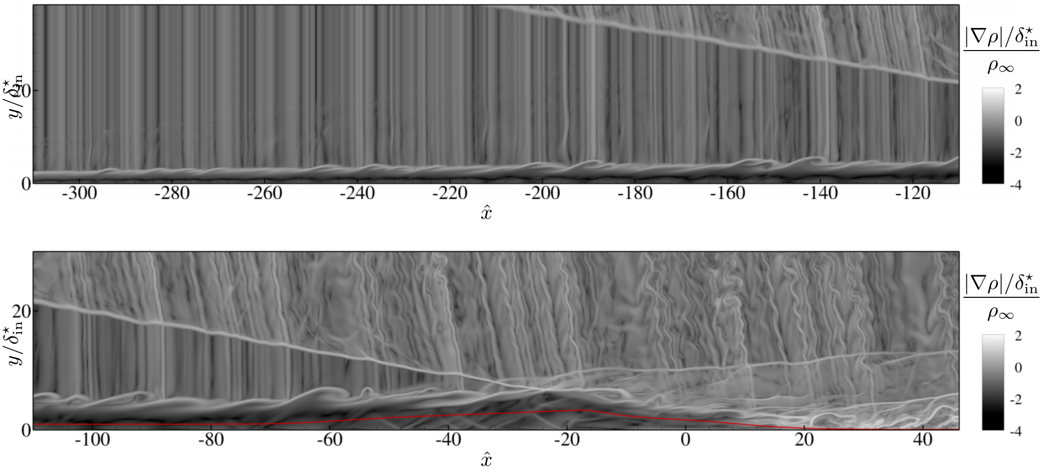

FIG. 11. Isocontours of normalized density gradient magnitude in an instantaneous *xy* slice of the computational domain in logarithmic scale.

relative to the phase speed of the instability, and is characterized by higher frequencies with respect to the first mode. In the past, both linear and weakly nonlinear stability studies [45,46] have pointed out that wall cooling tends to stabilize first-mode instability while destabilizing the second mode, which may even become the most unstable one at lower Mach numbers. Recently, many authors have observed the presence of such an instability in high-enthalpy flows as well [47–51]. Following the trend of the skin friction coefficient in Fig. 5, the flow behavior starts to deviate from the base flow self-similar solution at $\hat{x} \approx -50$. Therefore, in the upstream flow, existing considerations corroborated for flat-plate boundary layers can be extended to the present study. The instantaneous density gradient $|\nabla\rho|/\delta^\star_{\rm in}/\rho_\infty$ is shown in Fig. 11. Ropelike structures can be observed in the top panel, focusing on the region upstream of the interaction zone. Such structures are shown not be as regular and pronounced as those found for cone configurations in Zhu *et al.* [52] and [50], although this difference can be attributed to the specific perturbations used in the present study. Concurrently, the bottom panel of Fig. 11 shows acoustic waves that are trapped and reflected by the wall and near the sonic line, marked in red in the figure. Visualizations of streamwise and wall-normal velocity fields (not shown) have also revealed the presence of distinguishable structures having a wavelength of almost twice the local boundary layer thickness, a common characteristic of second

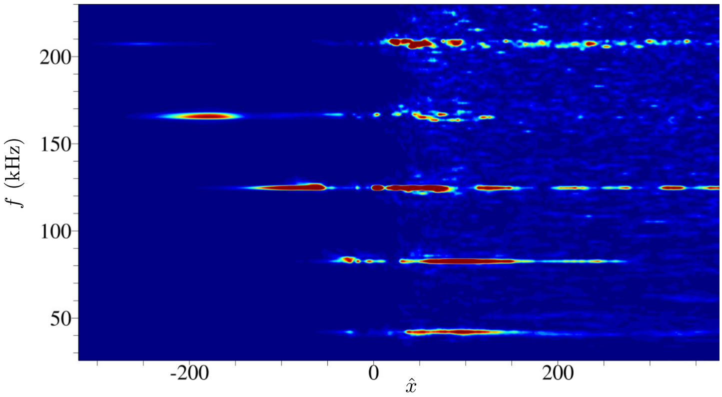

FIG. 12. Premultiplied power spectral density of the wall pressure in the interaction region.

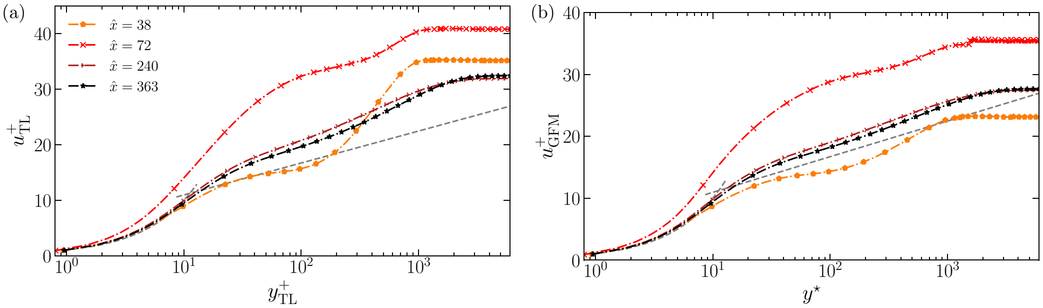

FIG. 13. Streamwise velocity scalings. Trettel and Larsson transformation (a) and Griffin-Fu-Moin transformation (b).

modes. Moreover, two-dimensional modes represented by roll-like shape structures near the wall are clearly visible in Fig. 4, extending up to the interaction zone.

From a more quantitative standpoint, the frequency of the Mack mode can be roughly estimated as $f_M = u_\delta/(2\delta_l)$ for low-enthalpy boundary layers [19], with δ_l the laminar boundary layer thickness. In the region of interest, comprised in $-200 \lessapprox \hat{x} \lessapprox -50$, such an estimation results in frequencies ranging between approximately 200 and 100 kHz. The Mack mode frequency basically decreases with increasing boundary layer thickness and, consequently, with increasing streamwise coordinate. It is evident that this estimate loses its validity when a clear boundary layer thickness cannot be distinguished anymore, such as in the interaction region. To analyze the frequency content of the flow, we show in Fig. 12 the premultiplied power spectral density (PSD) of the wall pressure for the streamwise region of interest. The predominant modes are explicitly excited by Eq. (19), the flow in this portion of the computational domain being still strongly influenced by the

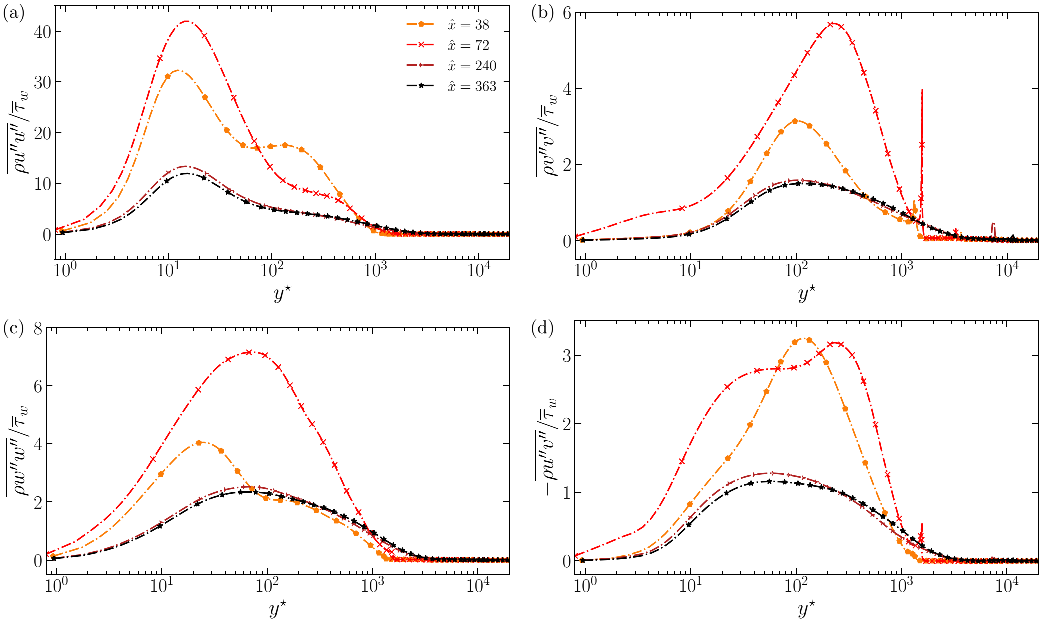

FIG. 14. Wall-normal profiles of the Reynolds stresses for the streamwise (a), wall-normal (b), spanwise (c), and shear (d) components.

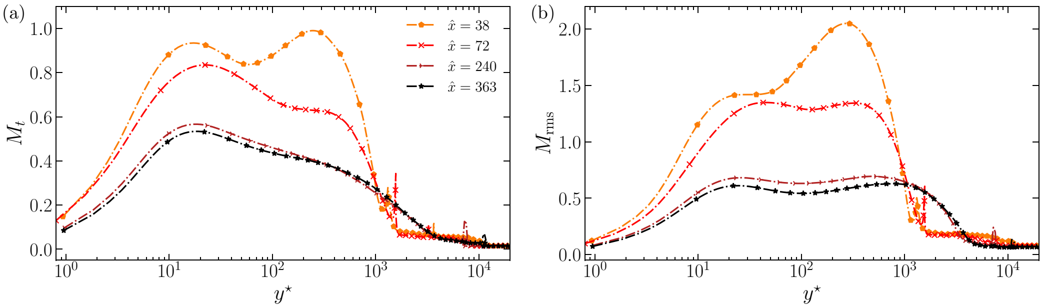

FIG. 15. Wall-normal profiles of turbulent Mach number (a) and r.m.s. Mach number (b) for the last four stations of Table I.

inflow forcing. Nevertheless, among all the frequencies excited through the perturbation function, specific frequencies emerge in the range comprising approximately between 50 kHz and 200 kHz. Before the impingement, a ≈160 kHz frequency is significantly predominant. Consistent with the boundary layer thickening downstream, the peak is then shifted to lower frequencies (≈125 kHz, 82 kHz). These results are in agreement with the f_M estimate; despite the region being still biased by the imposed disturbances, the closest frequency to f_M is naturally selected at each streamwise location and prevails among the others. When the boundary layer is subjected to the impinging shock, other mechanisms emerge and the spectrum starts to fill up, both sustaining the previously emerged frequencies and highlighting new ones. The large computational cost of the simulation limits the temporal window of sample collection, and therefore no information about low-frequency unsteadiness can be provided at the moment. Whether the bubble breathing phenomenon is present even when the shock impinges on a high-enthalpy transitional boundary layer will be the subject of future work.

C. Turbulent statistics

We present an overview of the main turbulent statistics at the last four stations of Table I. Note that an in-depth analysis of the turbulent flow over a thermochemical out-of-equilibrium boundary layer was already performed by Passiatore *et al.* [26]; the results here presented share similar trends. First, the transformations of Van Driest [53], Trettel and Larsson [54], and Griffin *et al.* [55] for the averaged streamwise velocity are applied to the transitional and fully turbulent stations. Figure 13 shows the results only for the last two scalings, both providing better predictions than the Van

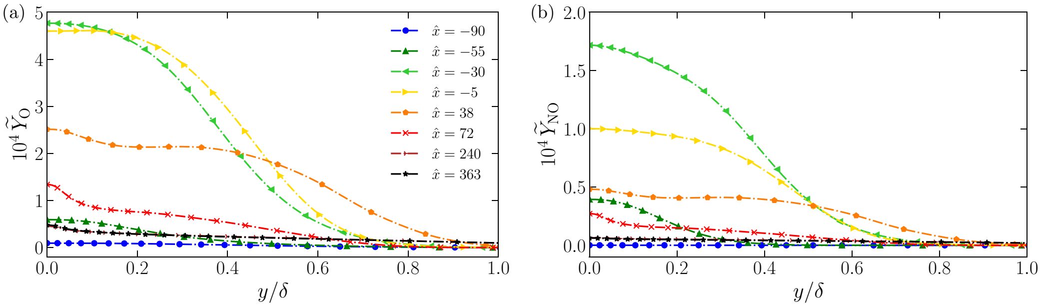

FIG. 16. Wall-normal distributions of atomic oxygen (a) and nitric oxide (b) for the different streamwise stations reported in Table I.

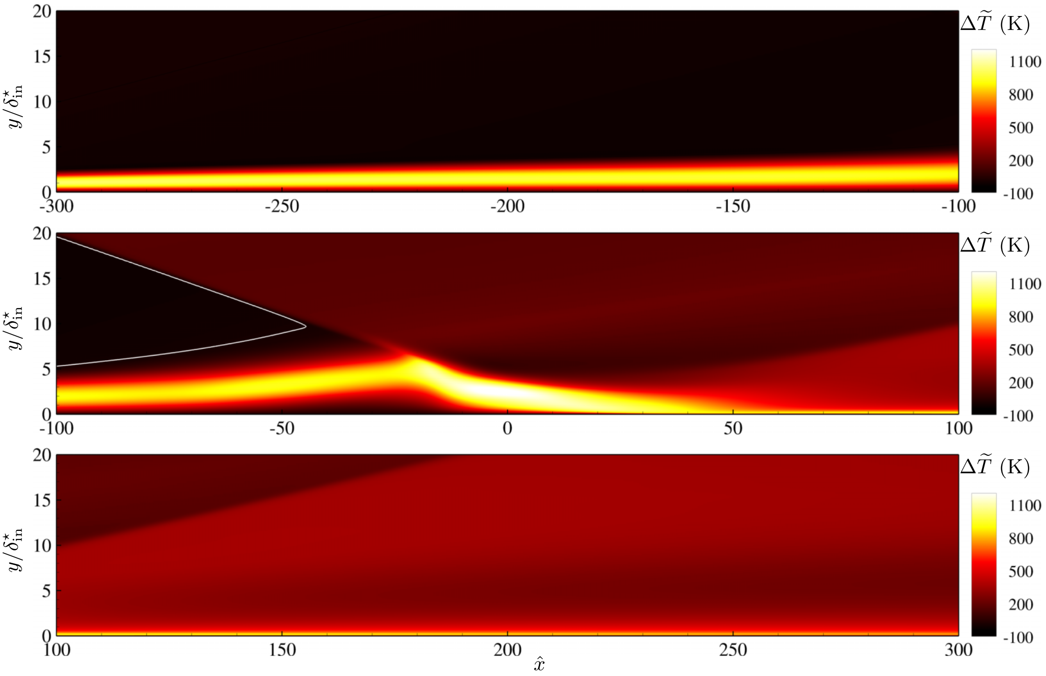

FIG. 17. Isocontours of the Favre-averaged dimensional temperature difference $\Delta\widetilde{T}$. The white line denotes the $\Delta\widetilde{T} = 0$ isoline. The y axis has been stretched for better visualization.

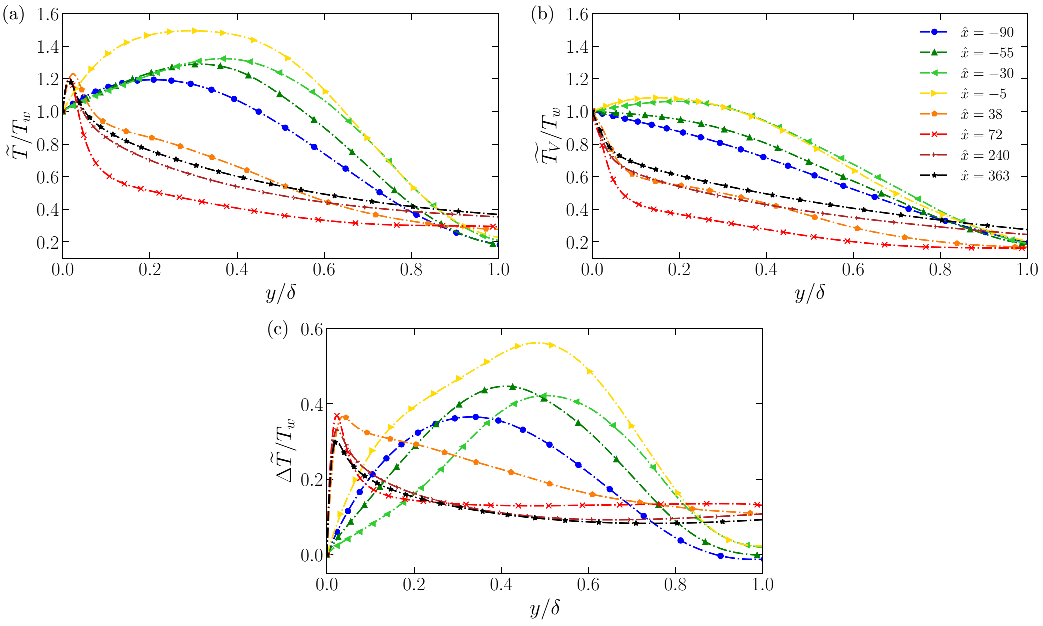

FIG. 18. Evolution of normalized mean rotranslational temperature (a), vibrational temperature (b), and temperature difference (c) in outer scaling.

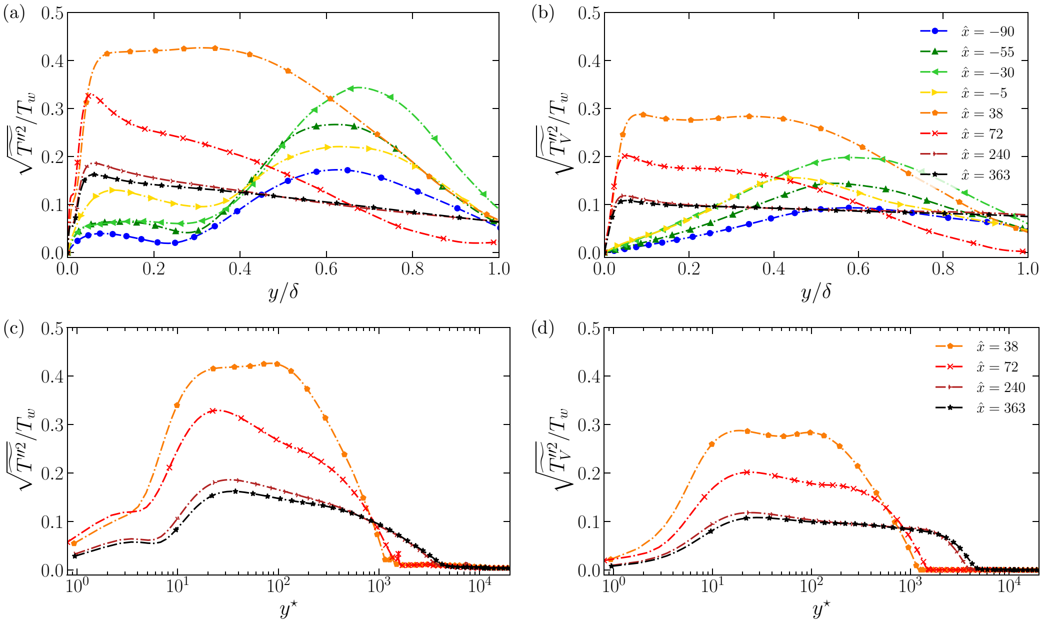

FIG. 19. Evolution of translational temperatures fluctuations [(a),(c)] and vibrational temperature fluctuations [(b),(d)], in outer scaling [(a), (b)] and inner scaling [(c), (d)].

Driest one. The collapse with the classical logarithmic profile is very poor for $\hat{x} = 38$ and $\hat{x} = 72$, confirming the purely transitional state of the boundary layer in this region. For the two last stations, these transformations fail to collapse the mean velocity profiles on the incompressible logarithmic law, as already observed by many authors [5,26,56]. It is of common agreement that the nominal Kàrmàn constant should be smaller than the classical value of ≈0.4, and the intercept should be greater than 5.2 at least for cooled boundary layers [23,27]. Reasonable self-similarity can be observed for the last two stations, the better collapse being obtained by the Griffin *et al.* [55] transform. The Reynolds stresses, shown in Fig. 14, exhibit a reasonable collapse when plotted in semilocal units, also due to the small changes in Re_τ for the two last streamwise positions (less than 10%). At the transitional stations, the flow is subjected to massive velocity and pressure fluctuations, two to three times larger than in the turbulent region. These lead to very large values for the turbulent Mach number, $M_t = \sqrt{\overline{u_i' u_i'}}/\overline{c}$, and the r.m.s. (fluctuating) Mach number, $M_{\mathrm{rms}} = \sqrt{\overline{M'M'}}$, shown in Figs. 15(a) and 15(b), respectively. M_{rms} is consistently larger than M_t at both the transitional and turbulent stations since it incorporates the effect of temperature fluctuations (through speed of sound fluctuations), which will be shown to be significant also in the outer region of the boundary layer. Furthermore, their values are similar to those obtained by Passiatore *et al.* [26] at much larger friction Reynolds numbers.

D. Thermochemical nonequilibrium

Before focusing the attention on vibrational excitation, we provide some insights on chemical activity. As already observed in previous works for cooled flat-plate boundary layers at similar freestream Mach numbers [25,26], chemical activity is relatively weak and scarcely influences flow dynamics. A more significant effect can be appreciated for pseudo-adiabatic [24] and adiabatic walls. Alternatively, when the freestream temperature is important (e.g., [27]) the influence of chemical activity is far from being marginal, the heat flux increasing due to species mass fraction fluctuations. For the present configuration, chemical dissociation is quite faint, reaching a peak of

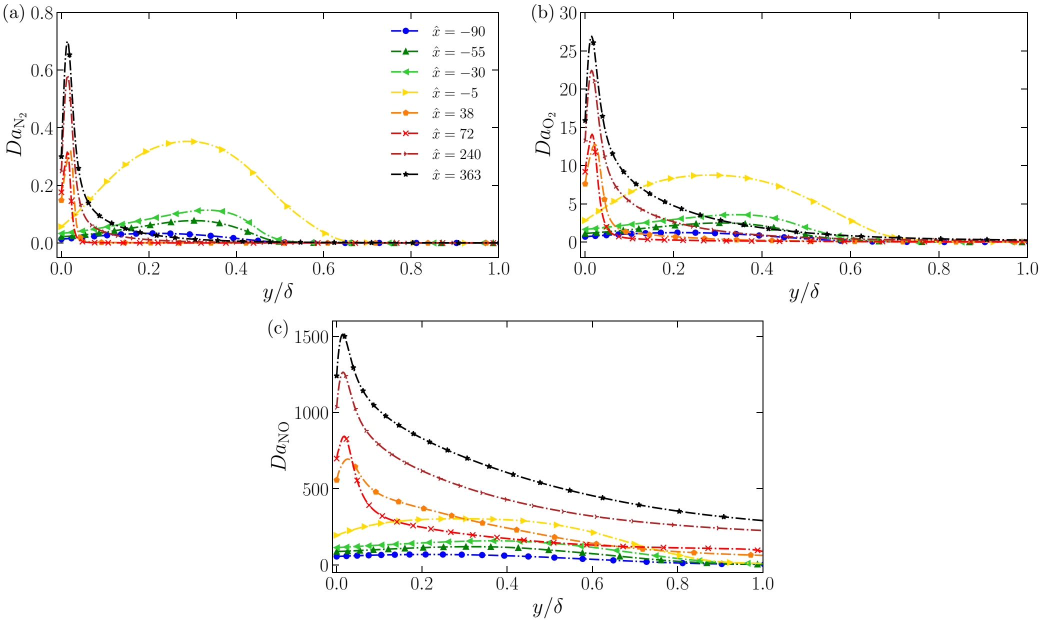

FIG. 20. Wall-normal evolution of vibrational Damköhler numbers.

atomic oxygen mass fraction of $Y_O \approx 5 \times 10^{-4}$, despite the relatively high temperatures registered. The wall-normal distributions of the chemical products at the different stations are shown in Figs. 16(a) and 16(b) for O and NO, respectively. Note that production of atomic nitrogen is negligible and will not be considered in the discussion. Notwithstanding the cooled boundary condition and the resulting nonmonotonic temperature profiles, the largest amount of chemical products is encountered at the wall in each region of the computational domain. The concentrations of species products increase passing from the laminar region to the interaction zone; when entering the recirculation bubble, where the temperature values are the largest, a rise up to an order of magnitude is registered, whereas their amount decreases in the transitional region. The distributions for the last two stations in the fully turbulent regimes are almost perfectly superposed because of the extremely low Damköhler numbers achieved here, highlighting a large difference between the characteristic timescales of turbulent motions and chemical activity. Such behavior is distinct from the one shown by Volpiani [28], in which chemical dissociation progressively increases reaching

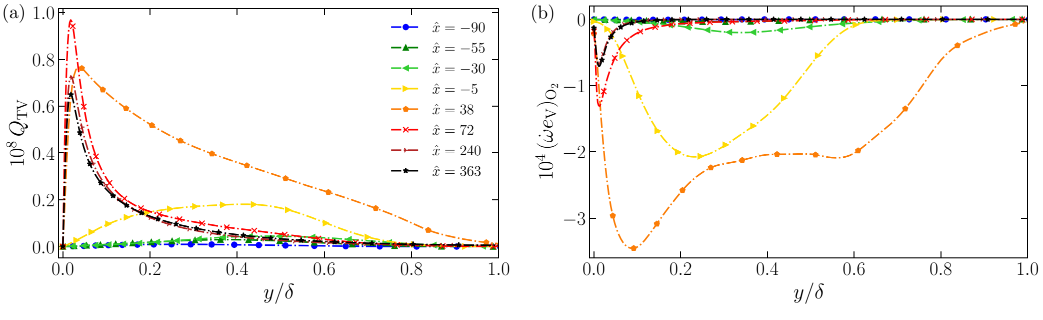

FIG. 21. Evolution of vibrational source terms. Translational-vibrational energy exchange (a) and chemical source term of O_2 (b). The quantities are dimensional, in W/m^3.

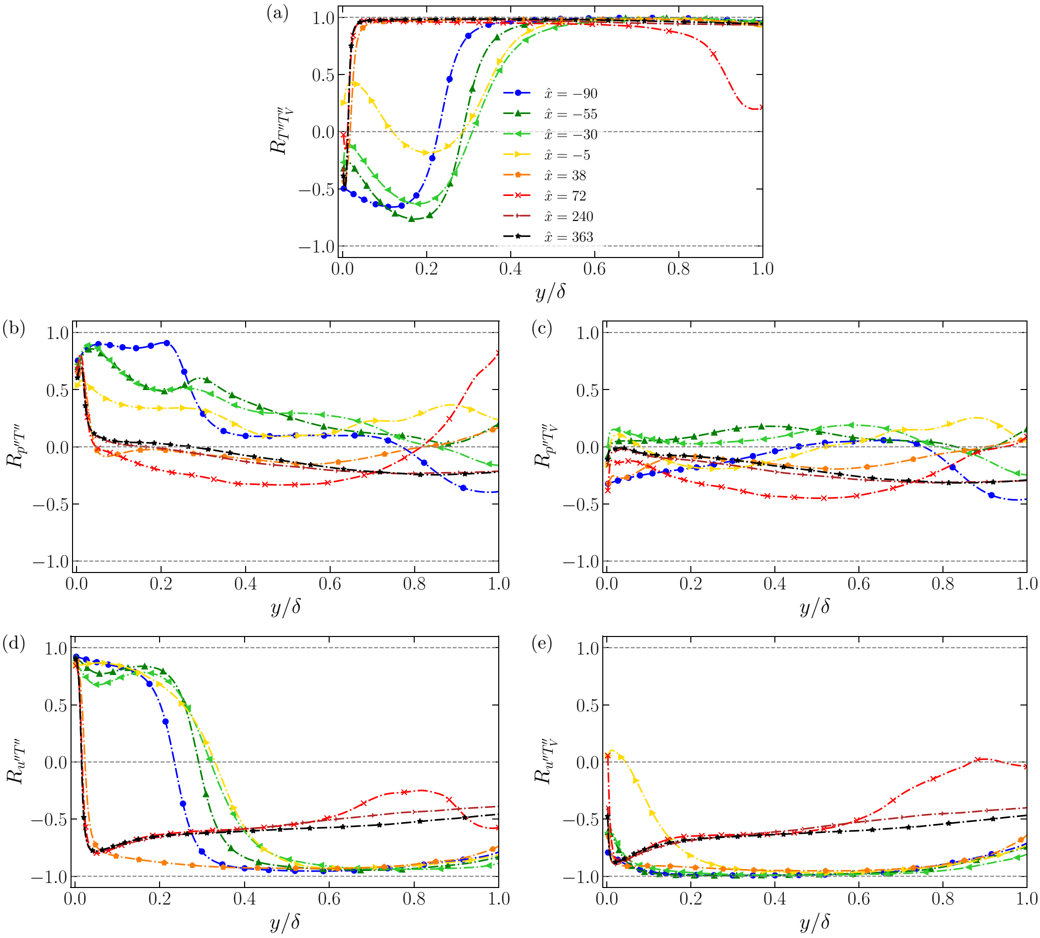

FIG. 22. Wall-normal profiles of correlation coefficients at the different stations listed in Table I.

a peak downstream of the interaction region. The difference can be ascribed to the much larger temperature values assigned at the wall and in the free-stream in that study.

Figure 17 reports the isocontours of the Favre-averaged dimensional temperature difference $\Delta\widetilde{T} = \widetilde{T} - \widetilde{T}_V$. The amount of thermal nonequilibrium is extremely high along the entire boundary layer, with maximum temperature differences larger than 1000 K registered in the interaction zone. The nonequilibrium state is mostly vibrationally underexcited, with $\widetilde{T}_V$ lagging behind $\widetilde{T}$ almost everywhere apart from the preshock freestream region. The two small overexcited flow pockets inside the recirculation bubble shown in Fig. 2 for the base flow disappear, although small $\Delta T < 0$ values are locally visible in the instantaneous flow field. To get further insights on the streamwise evolution of the thermal nonequilibrium, Fig. 18 displays the wall-normal profiles of $\widetilde{T}$, $\widetilde{T}_V$ and $\Delta\widetilde{T}$ in Figs. 18(a), 18(b), and 18(c), respectively, at the selected stations. Upstream of the impingement station, the profiles of the two temperatures keep distinct values due to the low Reynolds numbers, in accordance with the predictions of the locally self-similar solution downstream of the inflow section. Owing to the presence of a cooled wall, the translational temperature always exhibits nonmonotonic distributions. On the other hand, the profiles of $\widetilde{T}_V$ display a monotonic profile with a maximum at the wall, which is therefore vibrationally heating the flow, coherently with the vibrational wall heat flux evolution. Such a behavior is partially reversed in the bubble region, where the lower flow

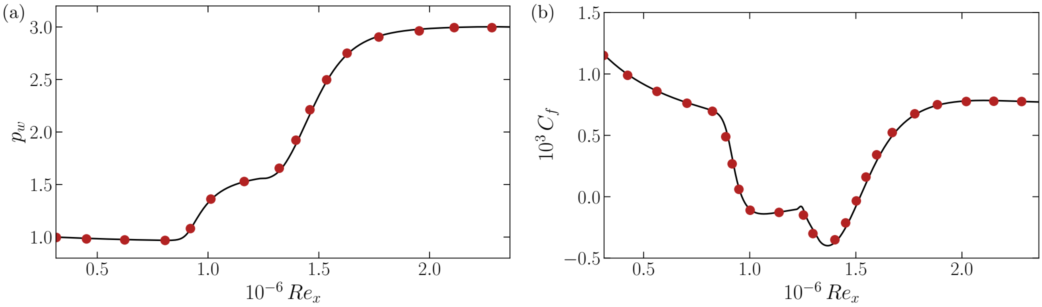

FIG. 23. Verification test cases for the two-dimensional SWBLI configuration. Evolution of normalized wall pressure (a) and skin friction coefficient (b), compared with the reference solution (symbols from [19]).

speed promotes a temperature increase to values higher than T_w. The largest absolute temperatures (as well as their difference) are registered at the reattachment point, with peaks of ≈3700 K and 2700 K for $\widetilde{T}$ and $\widetilde{T_V}$, respectively. Here the gap between the temperatures also reaches a maximum, and the wall-normal location of its peak is the farthest from the wall ($y/\delta \approx 0.48$, compared to $y/\delta \approx 0.32$ in the laminar region). From this station on, the peak is rapidly shifted towards the wall in the range $0.02 < y/\delta < 0.03$, due to the sudden decrease of the boundary layer thickness before, and the increase in turbulent activity after. In the last two stations, the turbulent mixing efficiently redistributes the gas [as shown in 26] such that the relaxation towards equilibrium of the vibrational modes is strongly delayed, resulting in a profoundly different dynamics with respect to the base flow predictions [29].

The evolution of the root mean square of the Favre fluctuations of rotranslational and vibrational temperatures is shown in Fig. 19 for all the stations in outer scaling, and in inner scaling for the streamwise position after the interaction region. The level of turbulent fluctuations is high even before the shock impingement, especially for the rotranslational temperature. The profiles of $\sqrt{\widetilde{T''^2}}$ in the fully turbulent region display two peaks, which are a local maximum at $y^\star < 10$ and a global maximum at $y^\star \approx 30$. These two peaks are more distinguishable when the temperature fluctuations are normalized with the corresponding Favre average [25,26]. The r.m.s. of the vibrational temperature present a radically different behavior, due to the particular trend of $\widetilde{T_V}$. The inner maxima registered for the rotranslational temperature at all the selected stations are smeared out for the vibrational one; moreover, vibrational fluctuations are less intense than their rotranslational counterparts everywhere. This is a direct consequence of the underexcited nonequilibrium persisting throughout the boundary layer, with T_V values lagging behind T ones. The severe thermal nonequilibrium state is confirmed by inspection of the vibrational Damköhler numbers computed with respect to the flow residence time,

$$\mathrm{Da}_m = \frac{x/u_\delta}{t_m}, \tag{24}$$

and shown in Fig. 20 for the three molecules of the mixture. While vibrational equilibrium is instantly reached for nitric oxide, molecular nitrogen and oxygen are shown to achieve nonequilibrium conditions in different regions. Specifically, $\mathrm{Da}_{\mathrm{O}_2}$ displays values of order unity in the outer part of the boundary layer ($0.3 < y/\delta < 0.5$), from the laminar region up to the recirculation bubble. The peaks are shifted towards the wall in the transitional region, and afterwards N_2 enters a nonequilibrium state with $\mathrm{Da}_{\mathrm{N}_2}$ values approaching unity towards the end of the computational domain. Figure 21 reports the two contributions to the vibrational energy variation, namely, the translational-vibrational energy exchange term Q_{TV} [Fig. 21(a)] and the variation due to chemical production and depletion $\dot{\omega}_m e_{Vm}$, shown only for molecular oxygen [Fig. 21(b)]. The absolute values of $\dot{\omega}_m e_{Vm}$ for N_2 and NO are even smaller and thus not shown. An order-of-magnitude analysis

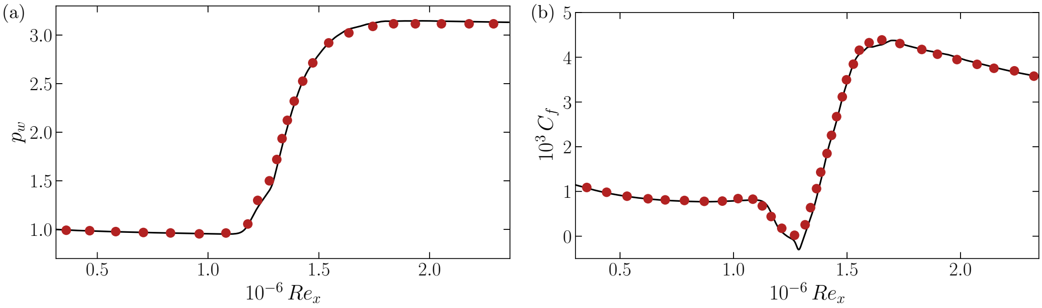

FIG. 24. Verification test cases for the three-dimensional perturbed SWBLI configuration. Evolution of normalized wall pressure (a) and skin friction coefficient (b), compared with the reference solution (symbols from [19]).

shows that e_V variations are almost uniquely due to translational-vibrational energy exchanges, which are particularly large in the transitional and fully turbulent regions. A high exchange rate is registered across the whole boundary layer thickness at $\hat{x} = 38$, which corresponds to the skin friction coefficient peak location and to the emergence of the energetic structures observed in Fig. 7. Here the maximum interaction with the chemical activity is also registered, its net effect being, however, negligible. Figure 22 shows correlation coefficients between the Favre-averaged fluctuations of different quantities. First, T'' and T_V'' are strongly correlated almost everywhere except close to the wall, where a slight anticorrelation is registered notwithstanding the same temperature values applied at the walls. This is again linked to the simultaneous vibrational wall heating and translational wall cooling, as shown by the wall heat fluxes and mean temperature profiles in Figs. 6 and 17, respectively. The trends of the correlations of p'', u'' (and v'', not shown) with T'' and T_V'' are qualitatively similar in the outer region of the boundary layer, while significant variations are observed for the inner zone. Specifically, $R_{p''T''}$ is shown to be predominantly positive (although in the turbulent region it tends rapidly to zero starting from the buffer layer), whereas p'' and T_V'' are loosely correlated highlighting the important decoupling between the internal vibrational and dynamic fields. The strong correlation observed for $R_{u''T''}$ in the near-wall region is not observed in the profiles of $R_{u''T_V''}$, which are shown to be strongly anticorrelated everywhere. Globally, T'' and T_V'' exhibit a drastically different behavior not only in the turbulent region (as previously shown by [26]) but also and above all in the interaction zone, where the amount of thermal nonequilibrium is the largest. Of note, the turbulent Prandtl and turbulent vibrational Prandtl numbers are ≈0.85 and 0.9, respectively, consistently with the values obtained for flat-plate boundary layers under largely different thermodynamic conditions [24–26].

VI. CONCLUSIONS

A Mach 9 shock-wave/transitional boundary layer interaction is investigated by means of direct numerical simulations. The present thermodynamic conditions are such that the boundary layer is thermally out of equilibrium, with effectively frozen chemistry. The impinging shock is generated by a wedge angle of $\vartheta \approx 5^\circ$, leading to a shock angle of $\beta = 10^\circ$; the resulting base flow is then perturbed with freestream inflow disturbances that are found to feed the classical Mack mode instability. Ropelike structures and two-dimensional modes are indeed recognized in the preshock region, with acoustic waves trapped between the wall and the sonic line even in the recirculation bubble. The dominant frequencies and wave lengths are also found to be in accordance with the second-mode instability. Concurrently, streaky structures are formed in the initial part of the domain but are then weakened by the shock impingement. The latter creates a much smaller separation region with respect to the unperturbed configuration. The combination of the instability mechanisms and incident shock is such that transition to turbulence is promoted only after the reattachment point.

This is clearly shown by the evolution of the skin friction coefficient, which exhibits a large increase due to the foot of the incident shock. The total wall heat flux follows approximately the same trend, albeit the vibrational contribution is one order of magnitude smaller than its rotranslational counterpart and mainly of opposite sign. The correlation between C_f and the Stanton number still stands, except in the interaction region. In the fully turbulent portion downstream of the impinging shock, turbulent statistics reveal reasonable self-similarity and corroborate the results previously obtained for turbulent boundary layers. Thermal nonequilibrium is quantified by means of mean and fluctuating temperature values, vibrational Damköhler numbers, and contributions of the vibrational source terms. Both molecular oxygen and molecular nitrogen exhibit vibrational excitation, but in different regions of the computational domain; namely, $\mathrm{Da}_{\mathrm{O}_2}$ is of order unity in the laminar region up to the recirculation bubble, whereas $\mathrm{Da}_{\mathrm{N}_2}$ attains similar values in the fully turbulent zones. Vibrational modes are found to be almost everywhere in an underexcited state, the largest amount of thermal nonequilibrium being achieved in the recirculating bubble. The correlation coefficients of the two temperatures with respect to p, u, and v drastically differ and highlight the important decoupling between the internal vibrational and dynamic fields.

The current study represents a first step towards the understanding of the influence of high-enthalpy effects on shocked turbulent flows, which were until now analyzed only in zero-pressure-gradient flat-plate boundary layer configurations. Future investigations on the subject will mainly focus on three different aspects: (1) the characterization of possible low-frequency unsteady motions detected by considering longer integration times, (2) the exploration of different regimes, in particular taking into account higher freestream total stagnation enthalpies, and (3) the analysis of the interaction with fully turbulent incoming boundary layers.

ACKNOWLEDGMENTS

This work was granted access to the HPC resources of IDRIS and TGCC under the allocation A0092B10947 made by GENCI (Grand Equipement National de Calcul Intensif). D.P. and G.P. were partially supported by the Italian Ministry of Education, University and Research under the Program Department of Excellence Legge 232/2016 (Grant No. CUP-D94I18000260001).

APPENDIX: VALIDATION

For the purpose of verification, we consider the configuration analyzed by Sandham *et al.* [19] of a shock wave interacting with a flat-plate boundary layer at Mach 6. The freestream conditions are $T_\infty = 65\,\mathrm{K}$, $p_\infty = 335.24\,\mathrm{Pa}$, $M_\infty = 6$; the wall temperature is fixed equal to $T_w = 292.5\,\mathrm{K}$. In order to minimize the differences with respect to the reference case, Sutherland's law is used to compute the dynamic viscosity with $T_{\mathrm{ref}} = 65\,\mathrm{K}$ and $\mu_{\mathrm{ref}} = 4.335 \times 10^{-6}\,\mathrm{Pa\,s}$, along with a constant Prandtl number equal to 0.72 and a specific heat ratio $\gamma = 1.4$. For the considered freestream conditions, a deflection angle of $\vartheta = 4^\circ$ generates a shock angle of $\beta \approx 12^\circ$. The shock impinges on the boundary layer at a distance from the leading edge equal to 0.344 m. The profiles of the similarity theory are imposed as inflow boundary condition at a Reynolds number $\mathrm{Re}_{x_{\mathrm{in}}} = 31.36 \times 10^4$, corresponding to $\mathrm{Re}_{\delta^\star_{\mathrm{in}}} = 6830$. The dimensions of the computational domain are $L_x \times L_y = 300\delta^\star_{\mathrm{in}} \times 35\delta^\star_{\mathrm{in}}$, discretized with 2400 and 300 grid points in the streamwise and wall-normal directions, respectively. A constant grid stretching is applied in the wall-normal direction. Figure 23 depicts the evolution of the normalized wall pressure and skin friction coefficient, respectively. The results are in excellent agreement with the reference data and faithfully reconstruct the pressure jump, the separation region, and the reattachment zone. We also have compared the results of the three-dimensional perturbed field. We have selected the case referred to as S-H by Sandham *et al.* [19]. The results reported in Fig. 24 show a quite acceptable agreement, and the transition to turbulence is well captured. In the present simulation there is a mild separation bubble with respect to the authors' results. Since the separation is extremely weak, this can be attributed to the statistical averaging of the skin friction coefficient. We also show in Fig. 25 the instantaneous

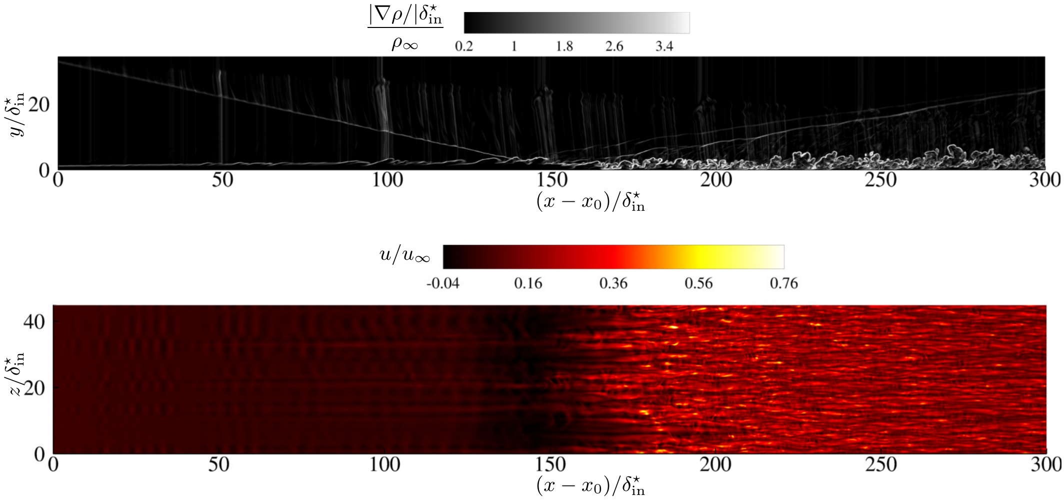

FIG. 25. Flow visualization. Numerical Schlieren (top) and normalized streamwise velocity in an *xz* plane near the wall (bottom).

flow field colored by of the numerical schlieren in a *xy* plane and the normalized streamwise velocity in a plane parallel to the wall. The results are in accordance with the imposed perturbation and with the analyses in Sandham *et al.* [19].

[1] J. Délery and J.-P. Dussauge, Some physical aspects of shock wave/boundary layer interactions, Shock Waves **19**, 453 (2009).
[2] G. Candler, Rate effects in hypersonic flows, Annu. Rev. Fluid Mech. **51**, 379 (2019).
[3] J.-C. Robinet, Bifurcations in shock-wave/laminar-boundary-layer interaction: Global instability approach, J. Fluid Mech. **579**, 85 (2007).
[4] N. Hildebrand, A. Dwivedi, J. W. Nichols, M. R. Jovanović, and G. V. Candler, Simulation and stability analysis of oblique shock-wave/boundary-layer interactions at Mach 5.92, Phys. Rev. Fluids **3**, 013906 (2018).
[5] L. Fu, M. Karp, S. T. Bose, P. Moin, and J. Urzay, Shock-induced heating and transition to turbulence in a hypersonic boundary layer, J. Fluid Mech. **909**, A8 (2021).
[6] Y. Andreopoulos, J. H. Agui, and G. Briassulis, Shock wave–turbulence interactions, Annu. Rev. Fluid Mech. **32**, 309 (2000).
[7] P. Dupont, C. Haddad, J. P. Ardissone, and J. F. Debieve, Space and time organisation of a shock wave/turbulent boundary layer interaction, Aerosp. Sci. Technol. **9**, 561 (2005).
[8] P. Dupont, C. Haddad, and J. F. Debieve, Space and time organization in a shock-induced separated boundary layer, J. Fluid Mech. **559**, 255 (2006).
[9] S. Pirozzoli and F. Grasso, Direct numerical simulation of impinging shock wave/turbulent boundary layer interaction at $m = 2.25$, Phys. Fluids **18**, 065113 (2006).
[10] M. C Adler and D. V Gaitonde, Dynamic linear response of a shock/turbulent-boundary-layer interaction using constrained perturbations, J. Fluid Mech. **840**, 291 (2018).
[11] M. Yu, M. Zhao, Z. Tang, X. Yuan, and C. Xu, A spectral inspection for turbulence amplification in oblique shock wave/turbulent boundary layer interaction, J. Fluid Mech. **951**, A2 (2022).
[12] H. Babinsky and J. K. Harvey, *Shock Wave-Boundary-Layer Interactions*, Cambridge Aerospace Series Vol. 32 (Cambridge University Press, New York, NY, 2011).

[13] N. D. Sandham, Shock-wave/boundary-layer interactions, NATO Research and Technology Organization (RTO) Educational Notes Paper, RTO-EN-AVT-195 (2011) pp. 1–18.

[14] G. Aubard, X. Gloerfelt, and J.-C. Robinet, Large-eddy simulation of broadband unsteadiness in a shock/boundary-layer interaction, AIAA J. **51**, 2395 (2013).

[15] N. T. Clemens and V. Narayanaswamy, Low-frequency unsteadiness of shock wave/turbulent boundary layer interactions, Annu. Rev. Fluid Mech. **46**, 469 (2014).

[16] P. S. Volpiani, M. Bernardini, and J. Larsson, Effects of a nonadiabatic wall on supersonic shock/boundary-layer interactions, Phys. Rev. Fluids **3**, 083401 (2018).

[17] P. S. Volpiani, M. Bernardini, and J. Larsson, Effects of a nonadiabatic wall on hypersonic shock/boundary-layer interactions, Phys. Rev. Fluids **5**, 014602 (2020).

[18] L. Vanstone, D. Estruch-Samper, R. Hillier, and B. Ganapathisubramani, Shock induced separation in transitional hypersonic boundary layers, in *43rd AIAA Fluid Dynamics Conference* (AIAA, San Diego, CA, 2013), p. 2736–2744.

[19] N.D. Sandham, E. Schülein, A. Wagner, S. Willems, and J. Steelant, Transitional shock-wave/boundary-layer interactions in hypersonic flow, J. Fluid Mech. **752**, 349 (2014).

[20] E. Schülein, Effects of laminar-turbulent transition on the shock-wave/boundary-layer interaction, in *44th AIAA Fluid Dynamics Conference* (AIAA AVIATION, Atlanta, GA, USA, 2014), Vol. AIAA, pp. 2014–3332.

[21] S. Willems, A. Gülhan, and J. Steelant, Experiments on the effect of laminar–turbulent transition on the SWBLI in H2K at Mach 6, Exp. Fluids **56**, 49 (2015).

[22] G. MD Currao, R. Choudhury, S. L Gai, A. J Neely, and D. R Buttsworth, Hypersonic transitional shock-wave–boundary-layer interaction on a flat plate, AIAA J. **58**, 814 (2020).

[23] L Duan and M. P. Martín, Direct numerical simulation of hypersonic turbulent boundary layers. Part 4. Effect of high enthalpy, J. Fluid Mech. **684**, 25 (2011).

[24] D. Passiatore, L. Sciacovelli, P. Cinnella, and G. Pascazio, Finite-rate chemistry effects in turbulent hypersonic boundary layers: A direct numerical simulation study, Phys. Rev. Fluids **6**, 054604 (2021).

[25] M. Di Renzo and J. Urzay, Direct numerical simulation of a hypersonic transitional boundary layer at suborbital enthalpies, J. Fluid Mech. **912**, A29 (2021).

[26] D. Passiatore, L. Sciacovelli, P. Cinnella, and G. Pascazio, Thermochemical nonequilibrium effects in turbulent hypersonic boundary layers, J. Fluid Mech. **941**, A21 (2022).

[27] J. Li, M. Yu, D. Sun, P. Liu, and X. Yuan, Wall heat transfer in high-enthalpy hypersonic turbulent boundary layers, Phys. Fluids **34**, 085102 (2022).

[28] P. S. Volpiani, Numerical strategy to perform direct numerical simulations of hypersonic shock/boundary-layer interaction in chemical nonequilibrium, Shock Waves **31**, 361 (2021).

[29] D. Passiatore, L. Sciacovelli, P. Cinnella, and G. Pascazio, A high-order scheme for the numerical simulation of high-enthalpy hypersonic flows, in *11th International Conference on Computational Fluid Dynamics, ICCFD 2022* (International Conference on Computational Fluid Dynamics, 2022) p. 1–17.

[30] C. Park, Two-temperature interpretation of dissociation rate data for N_2 and O_2, in *AIAA, Aerospace Sciences Meeting, 26th, Reno, NV, Jan. 11-14, 1988* (AIAA, 1988), p. 458.

[31] C. Park, *Nonequilibrium Hypersonic Aerothermodynamics* (John Wiley and Sons, 1990).

[32] R. C. Millikan and D. R. White, Systematics of vibrational relaxation, J. Chem. Phys. **39**, 3209 (1963).

[33] C. Park, Review of chemical-kinetic problems of future NASA missions. I–Earth entries, J. Thermophys. Heat Transfer **7**, 385 (1993).

[34] C. Park, Assessment of two-temperature kinetic model for ionizing air, J. Thermophys. Heat Transfer **3**, 233 (1989).

[35] F. G. Blottner, M. Johnson, and M. Ellis, Chemically reacting viscous flow program for multi-component gas mixtures, Technical Report No. SC-RR-70-754, Sandia National Laboratory, Albuquerque, New Mexico, 1971.

[36] J. O. Hirschfelder and C. F. Curtiss, *Molecular Theory of Gases and Liquids* (John Wiley and Sons, 1954).

[37] C. R. Wilke, A viscosity equation for gas mixtures, J. Chem. Phys. **18**, 517 (1950).

[38] T. Poinsot and D. Veynante, *Theoretical and Numerical Combustion* (R. T. Edwards, 2005).

[39] R. N. Gupta, J. M. Yos, R. A. Thompson, and K. P. Lee, A review of reaction rates and thermodynamic and transport properties for an 11-species air model for chemical and thermal nonequilibrium calculations to 30000 K, Report No. NASA-RP-1232, NASA, 1990.

[40] L. Sciacovelli, D. Passiatore, P. Cinnella, and G. Pascazio, Assessment of a high-order shock-capturing central-difference scheme for hypersonic turbulent flow simulations, Comput. Fluids **230**, 105134 (2021).

[41] S. Pirozzoli and M. Bernardini, Turbulence in supersonic boundary layers at moderate Reynolds number, J. Fluid Mech. **688**, 120 (2011).

[42] R. Quadros and M. Bernardini, Numerical investigation of transitional shock-wave/boundary-layer interaction in supersonic regime, AIAA J. **56**, 2712 (2018).

[43] C. Roy and F. Blottner, Review and assessment of turbulence models for hypersonic flows, Prog. Aerosp. Sci. **42**, 469 (2006).

[44] P. Andersson, L. Brandt, A. Bottaro, and D. S. Henningson, On the breakdown of boundary layer streaks, J. Fluid Mech. **428**, 29 (2001).

[45] A. V. Fedorov and A. P. Khokhlov, Prehistory of instability in a hypersonic boundary layer, Theor. Comput. Fluid Dyn. **14**, 359 (2001).

[46] N. Bitter and J. Shepherd, Stability of highly cooled hypervelocity boundary layers, J. Fluid Mech. **778**, 586 (2015).

[47] F. Miró Miró, E. S. Beyak, F. Pinna, and H. L. Reed, High-enthalpy models for boundary-layer stability and transition, Phys. Fluids **31**, 044101 (2019).

[48] L. C. Salemi and H. F. Fasel, Synchronization of second-mode instability waves for high-enthalpy hypersonic boundary layers, J. Fluid Mech. **838**, R2 (2018).

[49] L. Zanus, F. M. Miró, and F. Pinna, Parabolized stability analysis of chemically reacting boundary-layer flows in equilibrium conditions, Proc. Inst. Mech. Eng. G: J. Aerosp. Eng. **234**, 79 (2020).

[50] X. Chen, L. Wang, and S. Fu, Secondary instability of the hypersonic high-enthalpy boundary layers with thermal-chemical nonequilibrium effects, Phys. Fluids **33**, 034132 (2021).

[51] D. Passiatore, Direct numerical Simulations of hypersonic turbulent boundary layers with thermochemical nonequilibrium effects, Ph.D. thesis, HESAM Université, Politecnico di Bari (2021).

[52] Y. Zhu, C. Lee, X. Chen, J. Wu, S. Chen, and M. Gad-el Hak, Newly identified principle for aerodynamic heating in hypersonic flows, J. Fluid Mech. **855**, 152 (2018).

[53] E. R. Van Driest, *The Problem of Aerodynamic Heating* (ARC, 1956).

[54] A. Trettel and J. Larsson, Mean velocity scaling for compressible wall turbulence with heat transfer, Phys. Fluids **28**, 026102 (2016).

[55] K. P. Griffin, L. Fu, and P. Moin, Velocity transformation for compressible wall-bounded turbulent flows with and without heat transfer, Proc. Natl. Acad. Sci. USA **118**, e2111144118 (2021).

[56] C. Zhang, L. Duan, and M. M. Choudhari, Direct numerical simulation database for supersonic and hypersonic turbulent boundary layers, AIAA J. **56**, 4297 (2018).